Factors affecting thickness and frequency of turbidites triggered by earthquakes in Kumburgaz Basin, Sea of Marmara

Nurettin Yakupoğlu, Pierre Henry, Gülsen Uçarkuş, K. Kadir Eriş, François Demory, Christian Crouzet, M. Namık Çağatay

Factors Affecting Thickness and Frequency of Turbidites Triggered by Earthquakes in Kumburgaz Basin, Sea of Marmara

Nurettin Yakupoğlu[a], Pierre Henry[b], Gülsen Uçarkuş[a], K. Kadir Eriş[a], François Demory[b], Christian Crouzet[c] and M. Namık Çağatay[a]

(a) Istanbul Technical University, Geological Engineering Department, EMCOL Applied Research Center, Faculty of Mines, Ayazağa, 34469 İstanbul, Turkey

(b) Aix Marseille Univ, CNRS, IRD, INRAE, Coll France, CEREGE, Aix-en-Provence, France

(c) ISTerre, Université Savoie Mont Blanc, Université Grenoble Alpes, CNRS, IRD, Université Gustave Eiffel, 73000 Chambéry, France

Abstract

Submerged fault ruptures generate earthquake-triggered mass flow deposits, which are extensively used as a tool in subaqueous paleoseismology. In tectonically active deep sedimentary basins, such as the Sea of Marmara (SoM), these mass flow deposits are defined as turbidite-homogenite units (THUs), consisting essentially of a coarse basal part and an overlying homogeneous mud (homogenite). Detailed characterization of THUs is crucial in order to establish meaningful criteria to link these units with earthquakes events and to identify their transport routes and depositional mechanisms. Here, we combine µ-X-ray Fluorescence (µ-XRF), Anisotropy of Magnetic Susceptibility (AMS) and additional rock magnetism analyses of a 21-m long piston core from the Kumburgaz Basin of SoM to define the upper stratigraphic boundary of THUs with hemipelagic sediments and investigate the controls of hydrological changes on turbidite frequency and thickness over the last 15 kyrs BP. The sedimentary succession of this period includes a lower lacustrine and an upper marine unit with two Holocene sapropel intervals. The sequence is interrupted by a total of 70 THUs, characterized by a significant magnetic foliation related to the depositional setting rather than

the magnetic signature. Magnetic mineralogy of the coarse basal parts of THUs have more ferromagnetic particles than the overlying homogenites and background sediments. While the homogenite parts have a more constant mineralogy than the basal parts, they do not differ the background sediments.

Based on an event-free chronostratigraphic model derived from radiocarbon ages and the published age of lacustrine-marine (L-M) transition, the average THU occurrence intervals in the lacustrine (14.8-12.6 kyrs BP), lower sapropel (11.2-5.7 kyrs BP), upper sapropel (5.4-2.7 kyrs BP) and non-sapropelic part of the marine unit (2.7 kyrs BP-present) are 235 yrs, 287 yrs, 114 yrs and 160 yrs respectively. The average thickness of the THUs in the same units are 20.8 cm, 15.7 cm, 6.1 cm and 6.1 cm. The variability of average THU occurrence intervals and THU thicknesses are controlled by the sea level rise and salinity increase following the full marine connection of the SoM at 12.6 kyrs BP, which caused changes in slope stability, sediment composition and sediment deposition in different parts of the basin. Geomechanical properties of the lower sapropel appears to have been important in resulting long THU recurrence intervals and relatively high THU thicknesses.

Keywords: Subaqueous paleoseismology, Turbidite-Homogenite, Sea of Marmara, Kumburgaz Basin, Anisotropy of Magnetic Susceptibility

1. Introduction

Many years after rock magnetic studies led on marine sediments (Harrison & Funnell, 1964; Opdyke et al., 1966), similar approaches were done in subaqueous environments dealing with a broad spectrum of problems related to (a) instantaneous sedimentary processes (Hiscott et al., 1997; Ge et al., 2012; Campos et al., 2013; Stachowska et al., 2020), (b) major past-climatic events (Kruiver et al., 1999; Demory et al., 2005a; Drab et al., 2015a), and (c) environmental changes (and resilience of sedimentary environments) (Pozza et al., 2004; Franke et al., 2009; Akinyemi et al., 2013; Nizou et al., 2016). Instantaneous sedimentary processes include subaqueous landslides and mass-flows that result in deposition of debris flows, mudflows and turbidites. They can be triggered by earthquakes (Shiki et al., 2000; Nakajima and Kanai, 2000; Goldfinger et al., 2003, 2017; Beck et al., 2007), storm waves (Prior et al., 1989), hyperpycnal flows (Mulder and Syvitski, 1995), gas hydrate dissociations (Bourry et al., 2009), sediment overloading (Nemec, 1990; Chapron et al., 1999), volcanic eruptions (Cita and Aloisi, 2000) and floods (Beck et al, 1996). In tectonically active sedimentary basins, turbidite units are common and occur interbedded with hemipelagic or pelagic sedimentary sequences. The most common triggering mechanism of turbidites in such basins is the seismic activity of submerged fault systems (Goldfinger et al., 2011; Çağatay et al., 2012; McHugh et al., 2014; Avşar et al., 2015; Yakupoğlu et al., 2019; Gastineau et al., 2021). Hence, turbidites have been widely used as a tool in subaqueous paleoseismology in different settings, including in the Sea of Marmara (SoM) (Adams, 1990; Nakajima and Kanai, 2000; Shiki et al., 2000; Gorsline et al., 2000; Goldfinger et al., 2003, 2007, 2008, 2017; Sarı and Çağatay, 2006; Beck et al., 2007; Goldfinger, 2011; Çağatay et al., 2012; Drab et al., 2012, 2015; Eriş et al., 2012; Pouderoux et al., 2012a, 2012b; Gutiérrez-Pastor et al., 2013; Barnes et al., 2013; Polonia et al., 2013, 2017; McHugh et al., 2014; Moernaut et al., 2014, 2017; Patton et al., 2015; Avşar et al., 2015; Van

Daele et al., 2017; Yakupoğlu et al., 2019; Ikehara et al., 2020; Wils et al., 2020; Gastineau et al., 2021).

Seismically triggered turbidites commonly consist of a coarse basal part (T: Turbidite Body) and an overlying homogenous silt-clay size cap (H: Homogenite, muddy turbidite or turbidite tail), and commonly termed as turbidite-homogenite units (THU). The term homogenite broadly represents the "Bouma E" sublayer that contains homogenous mud deposited from the suspension cloud of a turbidity current. Thick (>1 m) homogenite layers can be imaged as seismically transparent facies in high-resolution seismic reflection profiles (Kastens and Cita, 1981; Cita and Rimoldi, 1997; Beck et al., 2007; McHugh et al., 2011; Eriş et al., 2012). However, homogenites are hardly distinguished from the overlying hemipelagic sediments using the usual physical and sedimentological properties such as gamma density and grainsize parameters (Çağatay et al., 2012; Eriş et al., 2012; Barnes et al., 2013; McHugh et al., 2014; Goldfinger et al., 2017; Yakupoğlu et al., 2019). These deposits have been recently best distinguished from the background hemipelagic sediments using the magnetic foliation determined from Anisotropy of Magnetic Susceptibility (AMS) measurements (Ge et al., 2012; Campos et al., 2013; Petersen et al., 2014; Tamaki et al., 2015; Rapuc et al., 2018; Stachowska et al., 2020). A clear demarcation of these boundaries is important for construction of a robust age-depth model based on an event-free stratigraphy, which can then be used dating THUs and establishing long-term paleoseismological records (Beck et al., 2009; Goldfinger, 2011; Barnes et al., 2013; Yakupoğlu et al., 2019),

The SoM, being located along the North Anatolian Fault (NAF), is an important location for subaqueous paleoseismological studies (e.g. Çağatay et al., 2012; Eriş et al., 2012; Drab et al., 2012; McHugh et al., 2014; Drab et al., 2015b; Yakupoğlu et al., 2019). Moreover, because of its interesting oceanographic setting between the Aegean (Mediterranean) Sea and Black Sea, its environment alternated between lacustrine and marine, with latest marine connection

93 taking place ~12.6 cal yrs BP and ensued sapropel formations during c.12.3 - 5.7 cal kyrs and
94 5.4 and 2.7 cal kyrs BP (Çağatay et al., 2015).

95 In this study, we integrate micro-X-Ray Fluorescence (μ-XRF) elemental geochemistry,
96 AMS and other rock magnetism analyses of a Calypso core (MRS CS-14) from the Kumburgaz
97 Basin of SoM with two main objectives: (1) to distinguish the boundary between the
98 homogenite layers of the THUs and overlying background hemipelagic sediments, and (2) to
99 understand how sea level and salinity rise control turbidite thickness and frequency during
100 different phases of the lacustrine and marine periods in the last 15 kyrs, based on a robust,
101 event-free age-depth model. Our findings from this integrated approach contribute to the
102 understanding of hydrological and seismotectonic controls on turbidite generation in a
103 tectonically active restricted basin, where tsunami generation (including reflection and seiche
104 effect) would be also expected (e.g. Beck et al., 2007; Çağatay et al., 2012: Ashi et al., 2014).

105 **2. Tectonic and oceanographic setting**

106 SoM is located in the NW part of Turkey and the western termination of the 1600-km
107 long NAF Zone. The deformation zone includes three main branches where northern and middle
108 branches of NAF are submerged faults systems within the SoM (Fig. 1). Based on GPS rates,
109 75 percent of the plate motion is transferred on the northern branch of NAF (NNAF) (~18-20
110 mm/yr) with the remainder being accommodated on the southern branches (Reilinger et al.,
111 1997; Straub et al., 1997; McClusky et al., 2000; Le Pichon et al., 2001; Armijo et al., 2002;
112 Provost et al., 2003; Flerit et al., 2003; Şengör et al., 2005; Reilinger et al., 2006). NNAF passes
113 through three fault-controlled basins, which from west to east are Tekirdağ (−1133 m), Central
114 (−1268 m), and Çınarcık (−1276 m) basins, that are separated by the Western and Central highs
115 (Fig. 1).

116 The SoM is connected to the Black Sea and Aegean Sea via the Bosphorus and
117 Dardanelles straits, respectively (Fig. 1). This connection allows exchange of two water masses

of different salinities; Mediterranean water (~38.5 psu) and Black Sea water (~18 psu) results in a two-way water current system with a permanent pycnocline at -25 m in the SoM (Ünlüata et al., 1990; Beşiktepe et al., 1994; Chiggiato et al., 2012; Aydoğdu et al., 2018). Renewal time of the upper and lower water masses of the SoM is 5-6 months and 6-7 years, respectively (Beşiktepe et al., 1994). The fluvial water and sediment input to the SoM is mainly from its southern catchment region by Kocasu, Gönen and Biga rivers ($2.2x10^6$ t/yr suspended material) (EIE, 1993; Kazancı et al., 2004).

During the Late Quaternary glacial-interglacial cycles, the environmental conditions in SoM alternated between lacustrine and marine, being controlled by the sills depths in the Dardanelles and Bosphorus, currently at -65 mbsl and -35 mbsl, respectively (e.g. Çağatay et al., 2000, 2015, 2019; Eriş et al., 2007). The last reconnection of the SoM with the Aegean Sea is dated between 14.7 kyr (initial connection, Vidal et al., 2010) and 12.6 kyr BP (full connection, Çağatay et al., 2015) and with the Black sea at c. 9 kyr BP (Major et al., 2006; Ryan, 2007). After the last marine reconnection, two sapropels were deposited in the SoM: Lower Sapropel (12.3-5.7 kyr BP, Çağatay et al., 1999, 2003, 2015; Vidal et al., 2010) and the Upper Sapropel (5.4-2.7 kyr BP, Çağatay et al., 1999; Tolun et al., 2002).

Kumburgaz Basin, where the studied core is located, is a depression located on the Central High with maximum depth of 880 m. It is a 35 km long, 11 km wide, ENE-trending depression, covering an area of 160 km^2 and bounded by NNAF to its north (Fig. 1; Çağatay and Uçarkuş, 2019). Continental slope to the north is marked by two amphitheater-like canyons. The eastern canyon is located off Büyük Çekmece Lagoon. The rocks exposed in the catchment area of the Kumburgaz Basin include Paleozoic schists and meta-granites and the overlying Eocene reefal limestones and Oligocene-Miocene sandstones and mudstones (Alp, 2014; Dalgıç, 2004). The basin has a sedimentation rate (2 to 2.5mm/yr) for Holocene period but two to three times higher rates for the lacustrine late glacial period (~5.4 mm/yr) (Beck et al., 2007).

3. Material and methods

3.1 Cores and multi-parameter analyses

Two ~21-m-long calypso cores CS-01 (28.50362/40.87140; 834 mbsl) (Yakupoğlu et al., 2019 and see figures therein) and CS-14 (28.47740/40.85860; 820 mbsl) were recovered from Kumburgaz Basin during the 2014 EC FP7 MARsite project cruise by *RV "Pourquoi pas?"* (Figs. 1B, 2). The core CS-14 was split into 1-m-long sections (21 sections), and core sections were split into two halves. One half was photographed, visually logged sampled for rock magnetism analyses Istanbul Technical University (ITU) Eastern Mediterranean Centre for Oceanography and Limnology (EMCOL). Core sections were split into two halves. Another half is used for Non-destructive analyses at the ITU-EMCOL core analysis laboratory, using Itrax μ-XRF core scanner and Geotek Multi Sensor Core Logger (MSCL). The core scanner was used for elemental composition (Fe, K, Ca, Sr, Mn) and digital X-ray radiography, and operated at 1 mm resolution and 20 s measurement time, using a Mo X-ray tube powered at of 30 kV and 50 mA. The MSCL was used for gamma density (GD) measurements at 10 mm resolution (Figs. 4-6). Total Organic Carbon (TOC) (difference between total carbon and total inorganic carbon (TIC)) analyses were performed using a Shimadzu TOC/TIC analyzer at ITU-EMCOL. Before the analysis, samples were dried in a freeze-dryer and processed on an augite mortar. Thus, total carbon content was measured by burning the sample at 900°C in a catalytic combustion furnace. For total inorganic carbon content, samples were treated with 85% phosphoric acid under 200°C, and the evolved carbon dioxide was measured by the detector. TOC concentration is calculated as the difference between total carbon and total inorganic carbon content. The precision for TOC and TIC analyses were 2% at 95% confidence level. (Fig. 3).

3.2 Anisotropy of magnetic susceptibility and rock magnetism analyses

All magnetic measurements were conducted in the Rock Magnetic Laboratory of the CEREGE (Aix-Marseille University). A total of 879 samples were collected using 8 cm^3 plastic boxes directly pushed into the sediment. For those samples, AMS was measured using AGICO MFK1-FA Kappabridge. The magnetic susceptibility tensors deduced from AMS measurements are characterized by three principal components (χ_{max}, χ_{int} and χ_{min}) and angles (declination and inclination) defining their orientation in the split-core reference frame (Jelinek, 1981; Hrouda, 1982; Tarling & Hrouda, 1993). Additionally, magnetic lineation (χ_{max}/χ_{int}), magnetic foliation (χ_{int}/χ_{min}) and mean tensorial magnetic susceptibility ($\chi_m=(\chi_{max}+\chi_{int}+\chi_{min})/3$) were calculated for each specimen.

In order to characterize magnetic mineralogy, two types of laboratory remanent magnetizations were artificially imparted on 98 samples through the core: Anhysteretic Remanent Magnetization (ARM) and Isothermal Remanent Magnetization (IRM). ARM was produced in-line and measured with the SRM760R using a 100 mT alternating field with a bias field of 50 µT. The ARM was also measured after a demagnetization step of 30 mT (ARM_{30}). The ratio ARM_{30}/ARM deduced from ARM measurements is a magnetic grain size indicator valid for constant low-coercive magnetic fraction (Johnson et al., 1975; Rochette et al., 1992; Tarling & Hrouda, 1993; Stoner & St Onge, 2007; Campos et al., 2013; Nizou et al., 2016). Isothermal Remanent Magnetization (IRM) was acquired at 3 T, measured and then at 0.3 T in the opposite direction using a pulse magnetizer MMPM9 from Magnetic Measurements Ltd. From these measurements, S-ratio was calculated by using formula (1- $IRM_{-0.3T}$ / $SIRM_{3T}$)/2. S-ratio is a parameter of the relative abundance of high coercivity minerals with values close to 1 for magnetite and decreasing with increased proportion of high coercivity minerals (Bloemendal et al., 1992; Demory et al., 2005b).

3.3 Chronology and age-depth model

191 Accelerator Mass Spectrometry ^{14}C analyses of four samples were carried out at the
192 TÜBİTAK-MAM (İzmit-Turkey) Radiocarbon Laboratory. Hemipelagic sediment samples
193 from beneath the mass-flow units were wet-sieved, and >63 μm fractions were used to hand-
194 pick carbonate shell material under binocular microscope. Dated materials were epifaunal
195 benthic foraminifera, echinoderm spicules and occasionally bivalve shells, in addition to the
196 planktonic foraminifera. Care was taken to sample whole shells without evidence of reworking
197 and diagenesis. All samples were washed in distilled water and dried (at 40 °C) before the
198 analysis. Results were calibrated using Calib v7.0 software with Marine13 ^{14}C calibration curve
199 (Reimer et al., 2013) and a reservoir age correction of 390 ± 85 for marine (Siani et al., 2000)
200 and 900 ± 100 for lacustrine samples (Çağatay et al., 2015) (Table 1). Inclusion of benthic and
201 pelagic shells in the same sample would not affect the reservoir age because of the negligible
202 difference (6–7 years) between the residence time of upper and lower water masses in the SoM
203 (Beşiktepe et al., 1994). In addition to the calibrated ages, we used the previously dated
204 lacustrine-marine (L-M) transition as dating point for the age-depth modelling (Table 1). The
205 two sapropel layers in the core were defined in 2.3-5.9 mbsf and 6.3-15.4 mbsf intervals, using
206 mainly by TOC analysis, as well as lithological and physical properties (Fig. 4), and were
207 previously dated by several authors in the SoM (Çağatay et al., 1999, 2003, 2015; 2019; Tolun
208 et al., 2002; Vidal et al., 2010; Filikçi et al., 2017). L-M transition in the SoM was previously
209 dated to be between 14.7 cal kyrs BP (for the initial connection) and 12.6 cal kyrs BP (full
210 connection) (Çağatay et al., 2015; Vidal et al., 2010). The L-M transition is marked by a 30 cm-
211 thick coarse shelly sand layer between 17.18-17.48 mbsf in core CS-14, which is characterized
212 by high χ_m (450 10^{-6} SI) values and a positive Mn excursion (>800 cps) (Fig. 3; Section 4.1).

213 For the age-depth modelling of core CS-14, all THUs thicknesses were discarded to
214 obtain an event-free composite depth, and all calibrated ages were processed with R-studio

using the script "CLAM" non-Bayesian method (Blaauw, 2010). The script created age-depth model, calculating the 95% Gaussian confidence interval around the best model (Fig. 4).

4. Results

4.1 Core lithology and geochemistry

The 21 m-thick sedimentary sequence in core CS-14 consists of a lower lacustrine unit and an upper marine unit on the bases of lithology, color, physical properties and fossil content (Figs. 2-4; Table 1). The boundary between the two units is located at c. 17.18 mbsf and the entire core sequence includes 70 THUs.

The marine unit is characterized by grey-green clayey-silty mud containing marine euryhaline molluscs, and benthic and planktonic foraminifera (Fig. 3). The uppermost ~2.3 mbsf of the marine unit contains homogenous fine silty clay showing a gradual downward change in color from brownish (oxidized mud) to light olive gray mud intercalated with twelve thin (average of 6.1 cm) THUs (Fig. 3; Table 2). The background sediments in this topmost unit are deposited at a rate of 0.79 m/kyr, and characterized by high χ_m values (~200 10^{-6} S.I) and low TOC (<1%) (Fig. 4; Table 2). The marine interval between 2.3-5.9 meters contains an olive gray homogenous silty clay with an oily luster, having ~1-1.5 % TOC and relatively low χ_m (~20 10^{-6} S.I) values (Fig. 4; Table 2). According to its TOC content, the interval between 2.3-5.9 mbsf corresponds to the upper sapropel in the SoM (Çağatay et al., 1999, 2015; Tolun et al., 2002). This sapropel contains 21 silty TH units within the range of 2.4-14.5 cm (Figs. 3-5; Table 2). Event-free part of the sapropel is deposited 0.68 m/kyr. Below the upper sapropel, the marine unit between 5.9-6.3 mbsf is green grey mud intercalated with two THUs with average of 5.1 cm in thickness thus, having 1.2-1.8% TOC concentration and sedimentation rate of 0.95 m/kyr (Fig. 4; Table 2).

238 The underlying interval between 6.3-15.4 mbsf is relatively dark green grey, laminated
239 mud with an oily luster. It contains abundant Fe-monosulphide nodules and patches and high
240 TOC contents of up to 3 % (Figs. 3,4; Table 2). Considering its lithological properties, the 6.3-
241 15.4 mbsf interval is correlated with the lower sapropel which was previously identified in the
242 SoM by different workers (e.g., Çağatay et al., 2000; Tolun et al., 2002; Vidal et al., 2010). The
243 event-free sapropel unit was deposited at a rate of 1.12 m/kyr (Fig. 4;). This interval contains
244 21 THUs in range of 3.5 to 59 cm (Table 2).

245 The marine interval between 15.4-17.2 mbsf a homogenous green gray clayey-silty
246 marine mud with scarce Fe-sulfide nodules and benthic foraminifera and without oily luster and
247 laminations (Figs. 3,4). This unit contains up to 2.5 % TOC in the lower part, which is mainly
248 of terrestrial origin according to C/N and C-isotope analysis (Tolun et al., 2002). Event-free
249 (background part) of the unit is deposited at a rate of 0.96 m/kyr. In this interval, four THUs
250 composed of silty-clayey fractions are observed with average of 11.1 cm in thickness. (Table
251 2). The underlying interval between 17.18 - 17.48 mbsf is a brownish grey, coarse sand layer
252 that separates the overlying marine sequence from the underlying lacustrine sequence (i.e. L-
253 M transition) (Figs. 3). It contains large marine and lacustrine bivalve shell fragments, abundant
254 black Fe-monosulfides spots, mm-size pyrite concretions and secondary gypsum crystals, and
255 is characterized by a high (c. 700 cps) Mn pulse and up to c. 500 10^{-6} SI χ_m values (Figs. 3-5).
256 The lacustrine unit below 17.48 mbsf in the core consists of brownish light gray clayey-silty,
257 massive mud, including fresh-brackish bivalves (*Dreissena* sp.) intercalated with 10 THUs. The
258 unit have up to 51 cm thick THUs (average of 20.8 cm), with its event-free background
259 sediments deposited at a rate of 0.8 m/kyr (Figs. 3,4; Table 2).

260 **4.2 Sedimentology and geochemistry of turbidite-homogenite units**

261 A total of 70 THUs consisting of a basal coarse part and an overlying turbiditic mud
262 (homogenite) were identified based on lithological, physical and geochemical properties (Figs.

263 3-6). The lower boundaries of the coarse basal part of the turbidites with the underlying
264 hemipelagic sediments are commonly sharp showing no scour and fill structures indicating non-
265 erosional base (Fig. 6) except some sandy thicker THUs in lower sapropel and lacustrine phase
266 (Fig. 6). The abrupt lithological change between the lower coarse basal parts and the upper
267 homogeneous parts is detected in GD (gamma density), χ_m, Ca, Sr, Fe profiles and digital X-
268 ray radiography images (Figs, 3, 6). Starting from middle of the lower sapropel frequent,
269 positive Mn excursions occurs in the top 11 m part of the sequence and at the L-M transition
270 (Figs. 4, 6). The upper boundary of homogenites of most THUs with the overlying background
271 sediments are not clearly discernable visually and in the µ-XRF elemental profiles while some
272 THUs show decrease in Fe and Ca at the boundary (Fig. 6). In contrast, homogenite lower
273 boundaries are commonly marked by a sharp change from parallel, silty laminae of the coarse
274 basal parts to massive mud of the homogenites. Some THUs' basal parts in the core sequence
275 are stacked without the homogenite part or hemipelagic sediments in between (Fig. 3). The
276 homogenites consist mainly of massive, fine silty clay, and have lower GD values than the
277 coarse basal parts but slightly higher GD values than the hemipelagic sediments (Figs. 3, 6).
278 However, transition from the homogenites into the overlying background sediments are not
279 clearly visible in the digital radiographic images (Figs. 3,6). Details about the thicknesses of
280 the THUs and their coarse basal and homogenite parts in the different chronostratigraphic units
281 are described in Section 4.4.

282 **4.3 Magnetic properties of turbidite-homogenite units**

283 In order to better characterize the boundaries between the THUs and overlying
284 background hemipelagic sediments, and the magnetic signature of the different
285 chronostratigraphic units, we derived magnetic foliation, lineation and mean susceptibility
286 precursors from the AMS (Figs. 5, 6). First 10 mbsf show magnetic foliation values of ~1.03-
287 1.04, interrupted by positive spikes of the THUs (Fig, 5). The sequence between 10 to 17 mbsf

contains high background foliation values (up to 1.06), regardless of the THU positive spikes, compared to the lacustrine background sediments (17.4-21 mbsl; foliation: 1.02-1.03). (Fig. 5). We observe a stable background foliation trend throughout the core, which reveals the magnetic characteristics of the THUs with positive excursions. Regardless of the TH lithology, AMS displays positive anomalies both on the coarse basal and homogenite parts of the sequence, with similar foliation values of 1.04-1.10 and 1.04-1.06, respectively (Figs, 5, 6). The boundary between homogenite and overlying background sediment shows a sharp drop on magnetic foliation on most of the THUs (Figs. 3, 6). Magnetic lineation has very low values throughout the core (1-1.03) (Figs. 5,6). Only some THUs have relatively high lineation (>1.007) having a positive pulse in coarse basal parts (Figs. 3, 5, 6).

Analysis of 98 samples from the core provided S-ratio, SIRM, ARM_{30}/ARM ratios in order to determine the magnetic characteristics of the lithological facies (Fig. 5). Accordingly, three lithologically different sections are identified corresponding to the coarse basal parts (18 samples), homogenites (7 samples) and background sediments (13 samples). S-ratio of these samples provided a scarce distribution (0.93-0.99). First 7 m of the core have the lowest values (0.93-0.96) (Fig. 5). Rest of the core have high S-ratios (0.96-0.99). ARM_{30}/ARM profile shows a narrow distribution in the core (0.2-0.6; have 0.43 average) (Fig. 5). In 9-14 mbsf interval, ARM_{30}/ARM has the lowest values (down to 0.2). The SIRM is rather constant along the core with values of 1-2 mA m^{-1} (Fig. 5). Still, several positive increments are observed in first 2 m and 18-21 m interval (Fig. 5).

Three selected THUs (THUs, A, B, C) were studied in detail to display the magnetic characteristics of THUs and background sediments in the main lithological units (i.e. marine, sapropel and lacustrine) (Figs. 3, 5, 6). In THU-A, ARM_{30}/ARM values oscillate between 0.40-0.45 and S-ratio is between 0.95-0.98. Foliation, lineation and χ_m of the coarse basal part show

312 positive pulses (up to 1.06, 1.01 and up to 2.5k 10^{-6} SI, respectively). Homogenite part of THU-
313 A is characterized by a decreasing foliation trend (down to 1.02) (Fig. 6).

314 THU-B is an amalgamated turbidite containing an Fe-depleted coarse base, which is
315 overlain by a Ca-rich coarse sediment. In this interval, S-ratio has a decreasing trend (down to
316 0.96), whereas ARM_{30}/ARM shows increasing trend with values up to 0.3 (Fig. 6). In the
317 homogenite part of THU-B, the ratio shows an increasing trend from 40% to %80. Foliation
318 profile has a positive pulse at the top of the coarse basal part and a high stable value over the
319 homogenite (1.03-1.05), whereas lineation only has a positive pulse at the coarse basal part of
320 the unit (up to 1.01). In THU-B, χ_m have higher values than the overlying background sediments
321 (up to 60-80 10^{-6} SI) (Fig. 6).

322 In both coarse basal and homogenite parts of THU-C, ARM_{30}/ARM values range
323 between 0.35-0.65 and S-ratio shows a fluctuating trend between 0.97 and 0.99 (Fig. 6).
324 Foliation and lineation profiles give positive pulses in the coarse basal part of this THU, with
325 up to 1.1 and 1.03, respectively. In the homogenite part, foliation values range between 1.04
326 and 1.05), which are higher than those in the overlying background sediments (1.03-1.04) (Fig.
327 6). χ_m profile has a peak in the coarse basal part of THU-C (up to 250 10^{-6} SI) but low values
328 in the homogenite part (~50 10^{-6} SI) (Fig. 6).

329 **4.4 Average occurrence interval and thickness variation of turbidite-homogenite units in**
330 **different chronostratigraphic units**

331 The age-depth model of core CS-14, based on four Accelerated Mass Spectrometry ^{14}C
332 ages and one chronostratigraphic horizon (i.e. L-M transition) (Table 2), is presented in Fig. 4.
333 "Clam" cubic spline script of this model allows us to determine the individual ages of 70 THUs
334 in the core and their average occurrence interval (or event frequency) in the different
335 chronostratigraphic units, including the lacustrine and marine units and the two sapropel layers

(Table 2, Supplementary Table). According to the model, the sedimentary sequence of core CS-14 extends back to c.15 cal kyrs BP and hence, the lacustrine unit was deposited between 14.8 and 12.6 cal kyrs BP (Fig. 4). The model also provides ages for the lower and upper sapropels within intervals of 11.2-5.7 kyrs BP and 5.4-2.7 kyrs BP, respectively (Fig. 4).

Using the age model, we determined the average occurrence interval of the THUs in different chronostratigraphic units of the core CS-14, which were defined based on visual observations, µ-XRF elemental and AMS profiles (Table 2; Supplementary Table). The lacustrine unit deposited during a ~2.4 kyr interval in the core includes 10 THUs, with an average occurrence interval of 235 yrs (Figs. 3, 4; Table 2; Supplementary Table). During the 5.5 kyr long lower sapropel interval, 21 THUs were deposited with an average occurrence interval of 287 yrs. The Upper sapropel with a depositional period of 2.7 kyrs has 21 THUs deposited with 114 yrs of average THU occurrence interval. The recent marine interval above the upper sapropel contains 12 THUs with an average occurrence interval of 160 yrs (Table 2). The average THU thicknesses and their percentages in the same units, from bottom to top, are 20.8, 15.7, 6.2 and 6.1 cm, and 30, 38, 35, and 53 %, respectively. The coarse basal part-to-homogenite part (TB-TT) thickness ratio range from an average of 0.3 (range: 0.1-0.5, neglecting on outlier value of 0.9) in the lacustrine unit to 0.9 (0.5-1.2) in the non-sapropelic marine unit below the lower sapropel (Supplementary Table 1). A gradual increase is observed in the average TB-TT thickness ratio from the lower sapropel (average. 0.6; range: 0.3-1.2) through upper sapropel (0.7; 0.2-1.1) to the upper non-sapropelic marine unit (0.8; 0.3-2).

5. Discussion

5.1 Factors controlling the magnetic properties of lacustrine and marine units and sapropels

Chronostratigraphic units of core CS-14 sequence show significant variations in all magnetic parameters. The core spans to the last ~15 kyrs BP with the earliest ~2.4 kyrs representing the lacustrine unit (Figs. 3,4). It has higher SIRM values than marine and sapropelic sediments, which are possibly related to higher content in ferromagnetic minerals inferred by higher mean susceptibility and relatively higher foliation (Fig. 5). The shelly sand layer with positive magnetic susceptibility and foliation pulses marking the L-M transition is interpreted to be a debrite (Figs. 3-5). Such unusual layers at the transition were previously reported in sediment cores from elsewhere in the SoM, and interpreted to be due to carbonate shell accumulation, inorganic carbonate precipitation and microbial reactions induced by mixing of lacustrine and marine waters (Çağatay et al., 2009, 2015, 2019; Eriş et al., 2011, 2019; Filikçi et al., 2017).

Despite the presence of the two sapropelic layers, the marine facies are characterized by relatively low χ_m (<50 x10^{-6} SI) similar to the cores from the Çınarcık, Tekirdağ and Central basins (Beck et al 2007; Drab et al., 2012; 2015a). The exception to this is the high χ_m values (>120 x10^{-6} SI) for the upper 2.2 m of the core, which represents the active diagenetic (redox) zone including the oxidized layers (Figs. 4, 5). This oxidized layer is accompanied also with low S-ratio and high SIRM, suggesting hematite enrichment.

Lower sapropelic sediments have significantly lower ARM_{30}/ARM in comparison to the rest of the marine sediments, indicating larger magnetite grain size. Indeed, the high S-ratio and low ARM_{30}/ARM suggest accumulation of magnetite (Fig. 5). The upper sapropelic layer possess low TOC values (1 – 1.5%) compared to the lower sapropel (Fig. 4). This layer is characterized by low χ_m despite the increment of hematite contribution to the magnetic signal (lower S-ratio and higher SIRM) (Fig. 5). Relatively low TOC enrichment in the upper sapropelic layer explains the low degree of sulfurization of the iron oxides including hematite. Background foliation profile has low values in the lower sapropel supported by relatively low

384 χ_m (Fig. 5). Even though S-ratio indicates that upper sapropel layer contains a portion of
385 hematite, this could indicate that the magnetic signature is carried by both magnetite and
386 hematite in this interval (Fig. 5) (Drab et al., 2015a).

387 **5.2. Sedimentological, geochemical and magnetic properties of turbidite-homogenite**
388 **units: Demarcation between homogenite and background hemipelagic sediments**

389 Sedimentological, geochemical and physical (gamma density and lithology) properties
390 of the THUs in Kumburgaz Basin core CS-14 are quite similar with those documented from the
391 other basins in the SoM (McHugh et al., 2006, 2014; Beck et al., 2007; Çağatay et al., 2012;
392 Eriş et al., 2012; Drab et al., 2015b; Yakupoğlu et al., 2019). Overall background sediments
393 display more variability depending on facies than THU sediments.

394 The coarse basal part of THUs (Fig. 6A) in the marine unit is represented by parallel
395 lamination and a sharp basal contact with the underlying background sediments. The basal parts
396 have a higher magnetic susceptibility and higher content in ferromagnetic grains. In the marine
397 THU example (Fig. 6A), coarse basal part has stronger foliation and lineation than both the
398 homogenites and background sediment. All THU units in the non-sapropelic facies except some
399 thinner examples have higher foliation than the overlying background sediments (Figs. 3, 6).
400 However, the transition upward is often progressive, and may be difficult to pinpoint based on
401 AMS data alone. This is especially true for the thinner events as the maximum resolution of
402 AMS data is 2 cm. Therefore, we have also taken into account the radiographic images (pattern
403 changes light to dark) and geochemical elemental distribution of THUs (especially trends of Fe,
404 Ca and Sr) to define the upper boundaries more precisely. The positive magnetic foliation
405 anomaly is not entirely correlated to the variations of other magnetic properties (see Fig. 6;
406 ARM_{30}/ARM and S-ratio profiles). In average, the turbidite layers appear to have a slight (but
407 statistically significant) increase of ARM_{30}/ARM compared with both homogenites and

408 background sediments.. The distinction of homogenite-coarse basal unit is rather visible in the
409 core photographs and radiography (Figs. 3, 6) due to different depositional mechanisms (Beck
410 et al., 2007). In Gulf of Corinth, combination magnetic foliation and the rock magnetic
411 measurement s shows the boundaries between homogenites and overlying background
412 sediments on selected examples (Campos et al., 2013). Coarse basal units represent deposition
413 of clastic sediments that are transported by the head and body of a turbidity current. These
414 sediments are detritus, containing high amount of Fe-bearing minerals and reworked Ca- and
415 Sr-bearing fossil fragments (Fig. 6). In particular, the transition between coarse basal and
416 homogenite parts of the THUs are commonly enriched in Ca and Sr, indicating the presence of
417 biogenic carbonate material remobilized from the shelf and upper slope of the Kumburgaz
418 Basin (Figs. 1,2,6) (Eriş et al., 2012).

419 Coarse sandy basal parts of THUs in the sapropels have thick laminations and
420 commonly show undulated base contact indicating erosional contact with underlying
421 background sediments (Fig. 6B). In lower sapropelic unit, marine sediments possess lower
422 ARM_{30}/ARM, which are likely related to magnetic grain size variation and/or occurrence of
423 greigite,. THU units have comparatively higher ARM_{30}/ARM In the lower sapropel, the average
424 foliation of the background sediment is not systematically lower, and even sometime higher,
425 than that of the homogenites, but the higher variability of the foliation parameter in the
426 laminated sediment at the 2 cm sampling scale still allows making a distinction (Figs. 3,
427 5).Homogenites in the sapropels are rather thick (up to 80 cm) (Figs. 3,6; Table 2), and show
428 darker shade than the background sediments in most radiographic images and photography
429 (Figs. 3, 6B). Moreover, the χ_m is an additional proxy to mark the upper boundary in sapropelic
430 THUs (Figs. 3,6) with both χ_m and foliation, showing a sharp decrease at the boundary between
431 these units, as previously documented by Campos et al. (2013).

Basal parts of THUs in the lacustrine unit are commonly thicker and coarser than those of THUs in the sapropels and the upper marine unit (Fig. 6C). As in the THUs in the upper marine and sapropel units, these coarse basal parts are represented by high Sr counts generated by platy biogenic carbonate material (Fig. 6). ARM_{30}/ARM, SIRM and χ_m values in the lacustrine interval are in average larger than in the other facies (Fig. 3), but also display a high variability, while values in the homogenite remain homogeneous (Fig. 6). The lacustrine facies presents the sharpest foliation contrast at the top of homogenites, typically 1.06 to 1.02 across the boundary between the homogenite and the background sediment.

In summary, coarse basal parts of the THUs have more ferromagnetic particles than the homogenites and background sediments (Fig 6), suggesting that the magnetic signature is mainly controlled by the depositional environments (Fig. 5). The homogenite tends to be relatively homogenous in magnetic properties as in chemistry. However, the diagenesis plays an important role on magnetic grain size, as exposed by the variability of ARM_{30}/ARM values of the THUs (see sapropelic and lacustrine THU example in Figs. 6). The variability as a function of facies is higher for the background sediment than for the homogenites. As a result the ARM_{30}/ARM is lower in the background sediment than in the homogenites within the lower (laminated) sapropel facies, while the opposite is observed in the lacustrine facies (Figs. 3-6). SIRM and χ_m are also higher in the lacustrine background sediment indicating a higher content in ferromagnetic minerals. The sharpest contrast in magnetic properties and fabric between homogenites and background sediment is observed within the lacustrine interval. Similarly, distinct boundary between THUs and the background sedimentation are observed on Alpine lakes (Crouzet et a., 2019). On the other hand, contrast is minimal, or reversed, within the laminated sapropel interval. These observations suggest that magnetic mineralogy and/or grain size is one of the factors influencing the magnetic fabric. Yet, in Sea of Marmara, variations in magnetic foliation in THUs are related to the deposition from turbulent flows rather than the

457 magnetic mineralogy of the sediments (Campos et al., 2013). Homogenite units are deposited
458 from suspension clouds following the deposition of the coarse basal layers from a body of
459 turbulent flow, and differ from the overlying background sediment by having more
460 homogeneous and compact textures and higher density (Shiki et al., 2000; Beck et al., 2007;
461 Eriş et al., 2012; Polonia et al., 2013, 2017; Drab et al., 2015b; Van Daele et al., 2017;
462 Yakupoğlu et al., 2019). Absence of bioturbation may also be a factor as the laminated sapropel
463 appear to have relatively high (and highly heterogeneous) average magnetic foliation. Similarly,
464 thick homogenites in lacustrine and marine non-sapropel facies should be less affected by
465 bioturbation than background sediments and this could, regardless of mineralogy and
466 depositional processes, favor a contrast in magnetic fabric.

467 **5.3. Climatic and Hydrological Controls on Turbidite-Homogenite Frequency and**
468 **Thickness**

469 In general, the occurrence interval (or event frequency) and thickness of THUs in
470 different chronostratigraphic units are highly variable (Fig. 3; Table 2; Supplementary Table
471 1). The occurrence interval ranges from an average of 114 yrs in the upper sapropel to 235 yrs
472 in the lacustrine unit. Since we discarded the muddy hyperpycnal turbidites that may have been
473 triggered by floods and storm waves, the remaining THU units, with a coarse and laminated
474 basal part and a homogenous muddy upper part (homogenite), could be triggered by earthquake
475 shaking in the tectonically active SoM basins (Fig. 3) (e.g. see Çağatay et al., 2012; McHugh
476 et al., 2014; Drab et al., 2015b; Yakupoğlu et al., 2019).

477 Comparison of two piston cores (CS-01 and CS-14), which are ~ 2.5 km apart in the
478 Kumburgaz Basin, show that THUs in Late Holocene period are rather similar in terms of THU
479 event frequency, thickness and grain-size. However, the numbers of THUs deposited in the last
480 6 kyrs in the two cores are different; CS-01 and CS-14 contain 28 and 34 THUs respectively,
481 which correspond to average recurrence intervals of 220 and 150 years, respectively (Fig. 2).

Moreover, different units in core CS-14 has widely variable THU occurrence intervals, with the individual event intervals ranging from 37 to 1200 years (Supplementary Table 1). If it is presumed that these units are triggered with earthquakes, this high variability is inconsistent with the 200-250 yrs recurrence interval of historical Mw>7 earthquakes in the Marmara region (e.g., Ambraseys and Finkel, 1995; Parsons, 2004). THUs also show different thicknesses in different units of core CS-14 succession. These observations suggest that factors other than earthquake magnitude need to be considered in order to explain the temporal and spatial variability of THU occurrence and thickness in a given basin (e.g. Wilhelm et al., 2016; Ikehara et al., 2016, 2017, 2020). These include core location in relation to the basin morphology, sedimentation rate, sediment sensitivity to earthquake shaking, and sea level change and related paleoenvironmental changes.

The basin depo-centers are assumed to be the best locations for a complete THU record, potentially comprising the highest THUs thicknesses of gravity-driven sedimentary deposits (McHugh et al., 2006, 2014; Goldfinger, 2011; Patton et al., 2015). However, the difference in the number of THU units and average THU occurrence intervals between cores CS-01 and CS-14 in the Kumburgaz Basin can be explained by their accessibility to the sediment transport routes rather than the water depth (Figs. 1, 2). Core CS-01 is recovered at -834 m near the toe of the north eastern canyon (Fig. 1), whereas core CS-14 is recovered at -820 m near the basin center on a structural high between two depo-centers. Its central position in the basin, together with its accessibility to sediment input from both the northeastern and northern canyons and possibly the northwestern canyon, makes the location of core CS-14 ideal for recording the maximum number of turbidites (Figs. 1, 2). The common presence of several amalgamated turbidites in core CS-14 supports sediment transport and deposition by turbidity currents arriving from the two or three canyons (Supplementary Table 1).

506 Other factors, such as intensity of earthquake shaking, sedimentation rate, sensitivity of
507 the sediments to remobilization, and environmental factors (e.g. climate, sea/lake level, salinity
508 changes), appear to be important in THU frequency and thickness variations. In particular,
509 earthquake epicenter and magnitude, and the distribution of strong-motion parameters (e.g. the
510 peak ground acceleration: PGA) are believed to be important for generating turbidity flows (e.g.
511 Howarth et al. 2021 and references therein). Short average event intervals (e.g. average: 114
512 yrs in upper sapropel of core CS14) suggest that the earthquake magnitude threshold for
513 triggering turbidity currents may not be only limited to large events if there are efficient
514 sediment transport routes such as the steep northern slope (with up to 20-degree slope angles)
515 and canyon systems in the Kumburgaz Basin (Fig 1). This assertion is supported by the
516 occurrence of the turbidity currents triggered by the Mw 5.8 earthquake of Sept 26, 2019 in the
517 NE corner of the Central Basin (Henry et al., 2022). This raises the question if a remote but
518 strong earthquake, not necessarily in submerged context, may also trigger turbidites and
519 recorded in the sedimentary sequence. However, subaqueous paleoseismological data from the
520 Sea of Marmara (SoM) (e.g., Çağatay et al., 2012; Drab et al., 2012, 2015b; McHugh et al.,
521 2015) and historical earthquake data (e.g., Ambraseys, N.N., Finkel, C.F., 1995) suggests that
522 ground acceleration generated by onshore M=6-7.4 earthquakes east and south of the SoM with
523 epicenters more than ca. 50 km of the basins did not trigger turbidites. For example, some
524 earthquakes (e.g. 25 May 1719 earthquake with Ms=7.4 and 1754 earthquake with Ms=6.8 with
525 epicenters east of the İzmit Gulf) were not recorded in the sediments of the Karamürsel Basin
526 in the İzmit Gulf (Çağatay et al., 2012, p.356 and references therein).

527 The THU occurrence interval and thickness distribution in core CS-14 also indicates the
528 importance of environmental and hydrological factors such as sea level, sedimentation rate and
529 salinity changes. The lacustrine unit contains the thickest and coarsest (coarse sand in basal
530 parts) THUs in the core lithology with an average thickness of 20.8 cm and an event frequency

of 4.255 $kyrs^{-1}$ (i.e. average event interval: 241 yrs) (Table 2). It is also characterized by the highest total sedimentation rate (1.98 mm/yr) and lowest TB-TT thickness ratio of 0.3, with THUs forming 53% of the unit's thickness (Table 2; Supplementary Table 1). THU thickness in the unit, calculated as five-point moving average, decreases from 38 cm from 14.6 kyrs BP to 8.5 cm before the sapropel deposition at 11.2 krs BP (Fig. 7A). A parallel change occurs in THU fraction, calculated as five-point moving average of each THU thickness divided by total sediment thickness between two events, as well as in the event interval (Fig 7B, C); the THU fraction ranges up to 73 % in the lower part of the lacustrine unit, but decreases to 35 % in the upper part of the lacustrine unit and in the marine unit below the lower sapropel and the five-point moving average event interval changes from ~250 yrs to 95 years (Fig. 7C). The high sediment input in the Kumburgaz basin during the Late Glacial period can be explained by the fact that, water level of the Marmara "lake" was below the Dardanelles Strait's sill depth, but gradually increase to -85 m just before the marine reconnection at ~12.6 kyrs BP (Figs. 1,3,4) (Çağatay et al., 2003; 2015; Eriş et al., 2011). Hence, the shelf was largely exposed during the deposition of the lacustrine unit until ~13.5 kyrs and fluvial sediment input from the Büyük Çekmece drainage network was directly delivered to the shelf edge and slope en route to the deep basin by gravity flow deposits. However, a decrease in the sediment input occurred during the 13.5-12.6 ka BP, which is likely to be due to a lake level increase.

Slope instability may have been another likely factor for THU events during the lacustrine period. Based on Cl^{-}, O and H isotope analyses of pore waters and a transport model, Aloisi et al. (2015) estimated the salinity of ~4 psu for the Marmara "lake" waters before the marine reconnection. Under such lacustrine fresh-brackish conditions together with low sea level provides hydrostatic pressure change on sediments, which deposited along the canyon and basin slopes would have been relatively unstable and may have further contributed to the thick THU deposition and low TB-TT thickness ratio in the Kumburgaz Basin.

After the full marine connection at 12.6 kyrs BP, the salinification of the SoM deep water was rapid, reaching the present levels within 1-2 kyrs of the connection (Çağatay et al., 2009; Aloisi et al., 2015), which possibly contributed to the stability of the slopes and reducing the canyon activity. The lower sapropel was deposited during 11.2-5.7 kyrs interval. The sea level rose from -85 m at 12.6 kyrs BP to the present sea level ~6 kyrs BP, before the end of the lower sapropel deposition (Grant et al., 2012). The total sedimentation rate was relatively high (1.68 mm/yr) with the THUs forming 35% of the sapropel thickness. High sedimentation rate for this period could have resulted from: (1) a wet and warm climatic condition with a high fluvial input (Caner and Algan, 2002; Mudie et al., 2002; Valsecchi et al., 2012), and (2) salinity-derived flocculation of clay-size fluvial material (Gibb, 1983; Wilkinson et al., 1997). However, this process is expected to enhance clay settling near river-marine water mixing zones, but with the relatively lower sea level, the mixing zone close to the shelf edge and a larger flux of hemipelagic sediment was settling out of suspension in the basin.

The lower sapropel includes relatively thick THUs with an average thickness of 15.7 cm and average TB-TT thickness ratio of 0.6 (Supplementary Table 1). THUs in this unit were deposited with the lowest frequency of 3.484 events $kyrs^{-1}$ (i.e. longest average event interval of 287 yrs) in the sequence (Table 2; Supplementary Table 1). Five-event moving average THU thickness in this unit ranges between ~40 cm and 6 cm, while average fractional thickness varies between 20 % and 40 %, with a decrease in both parameters towards the top of the unit (Fig. 7A, B). The THU event interval is ~700 years for the main part of the unit but decreases to ~150 years in the upper quarter part (Fig. 7C). Hence, the THU fraction in the lower sapropel is much lower and the THU event interval is considerably longer than those in the lacustrine unit. Moreover, the basal parts of THUs within the lower sapropel are finer in grain size and TB-TT thickness ratio is higher than that of THUs of the lacustrine unit.

580 The main control on the long event interval and grain size of THUs in most part of the
581 lower sapropel appears to be the cohesive and relatively high shear strength of sapropels, which
582 result from particle bonding between the organic matter and in situ organic and clay fabrics that
583 develop by deposition from anoxic water column (Kopf et al., 1998; Obuka et al., 2015). Such
584 geomechanical properties would require a relatively large earthquake shaking (strong-ground
585 motion) to trigger turbidity currents from the basin slopes. Long intervals between the turbidite
586 events in turn allowed thick sediment accumulation (sediment loading) on the slope and shelf
587 edge, which was consequently remobilized by earthquake shaking, resulting in the relatively
588 thicker THUs, with relatively higher TB-TT thickness ratios in the sapropel unit. This
589 conclusion is supported by similar trends of the THU thickness and event interval profiles for
590 almost the entire core section (Fig 3; Table 2).

591 The rising sea level was stabilized towards the end of the lower sapropel deposition, and
592 the sedimentation rate, THU thickness, and event recurrence interval decreased, and the TB-TT
593 thickness ratio increased towards end of the upper sapropel deposition and during the ensuing
594 marine (5.7-5.4 kyrs BP), upper sapropel (5.4-2.7 kyrs BP) and recent marine (2.7 kyrs BP to
595 present) depositional intervals (Fig. 7A, C; Table 2; Supplementary Table 1). The transition to
596 low sedimentation rates and gradual increase in the TB-TT thickness ratio starting from ~7 kyrs
597 BP was mainly due to rise in sea level (Fig. 4), which caused most fluvial sediments to be
598 trapped in the Büyük Çekmece Lagoon and near coastal areas, rather than reaching to the shelf
599 edge, slope and basinal areas. Only small amounts of fine sediments would have been
600 transported by currents to accumulate on the slopes, and subsequently mobilized en route to the
601 basin to be deposited as thin (6-7 cm-thick) and largely muddy THUs at high frequency in the
602 upper sapropel and latest marine units, as indicated also by the relatively low TB-TT thickness
603 ratio (Fig 3, Table 2; Supplementary Table 1). Indeed, the frequency of THU occurrence in the
604 two units, and in particular in the upper sapropel, is higher than the underlying lower sapropel

and lacustrine units. This is mainly due to the sensitivity of these marine sediments to earthquake shaking because of their lower TOC content, compared to that of the lower sapropel, and to their deposition under high sea level, compared to the lake level during the deposition of the lacustrine unit.

The upper sapropel and the recent marine unit show some fluctuations in the turbidite thickness, turbidite fraction and event interval (Fig. 7), which are likely due to artefacts in the age model (e.g. two radiocarbon ages in a short interval). However, some differences may be related to environmental conditions; upper sapropel was deposited with slightly higher organic productivity and under relatively lower bottom-water oxygen conditions than the recent marine unit, as indicated by the TOC and Mn profiles (Fig. 4). These differences are reflected in the relatively higher total and background sedimentation rates, lower TB-TT thickness ratio and shorter average event interval of the upper sapropel unit than those of the recent marine unit (Table 2).

6. Conclusions

Geochemical and rock magnetic parameters of core CS-14 from Kumburgaz basin enable us to provide a more accurate determination of the THU boundaries within the last 15 kyrs BP. THUs deposited in marine (including Holocene sapropels) and lacustrine facies of the core show different characteristics in terms of thickness, grain size, geochemical and magnetic aspects. These differences are mainly related to the sensitivity of sediments to remobilization, core location and hydrological conditions related to both the sea level and salinity rise subsequent to the full marine connection of the SoM. In 15 kyrs-long sedimentary record includes different lacustrine and marine, including Holocene sapropels, are characterized by lithological and geochemical precursors (TOC, µ-XRF). A robust event-free age-depth model was constructed to date the units and determine the frequency (event interval) of THUs.

Boundaries between homogenites and overlying background sediments are well-defined by *AMS* (magnetic foliation). The magnetic foliation shows strong positive pulses in THUs in every facies indicating that its trend is related to the changes in depositional setting and to the rising sea level rather than the magnetic signature of THUs and hemipelagites. Based on the age-depth model of the core, average THU occurrence intervals in marine (2.7 kyrs BP-present), upper sapropel (5.4-2.7 kyrs BP), lower sapropel (11.2-5.7 kyrs BP), marine (12.6-11.2 kyrs BP) and lacustrine units (15-12.6 kyrs BP) are ~160 yrs, ~114 yrs, ~287 yrs, 246 yrs and ~235 yrs, respectively.

Results of this study enhance our understanding of turbidite generation and its use in subaqueous paleoseismology. Short THU intervals of upper sapropel and the most recent marine sequence suggest the possibility of turbidity current triggering and THU deposition by moderate magnitude earthquakes (5-6.5 Ms). Several environmental factors (climatic and hydrological), together with seismic activity, affect the deposition of THUs, and should be considered in subaqueous paleoseismological studies. In particular, sensitivity of sediments to remobilization during earthquake shaking, together with hydrological (sea level and salinity), changes are considered to be of critical importance in understanding the conditions of turbidite generation, and therefore, in paleoseismological studies in the Sea of Marmara and similar marine/lacustrine settings.

Data Availability

Global sea level dataset related to this article can be found at https://doi.org/10.1038/nature11593 an open-source online data repository hosted at https://www.nature.com/articles/nature11593#Sec3 (Grant et al., 2012).

All sediment core datasets related to this article can be found at http://www.emcol.itu.edu.tr/Icerik.aspx?sid=13881 an online data repository.

Acknowledgments

This study is part of Nurettin Yakupoğlu's PhD Dissertation. Cores were taken during MARSITECRUISE of Ifremer/Genavir R.V.Pourquoi Pas?, within the framework of MARSITE FP7 EU Project (grant agreement no.: 308417). Financial support was provided by the bilateral ANR/TUBITAK collaborative research project MAREGAMI (ANR-16-CE03-0010-02 and Tubitak Project 116Y371). Part of this work has been supported by TÜBİTAK 1002 project (118Y057) and ITU BAP project (MDK-2020-42743). All geochemical and sedimentological analyses were performed in ITU EMCOL laboratories.

References

Adams, J., 1990. Paleoseismicity of the Cascadia subduction zone: evidence from turbidites off the Oregon-Washington margin. Tectonics 9 (4), 569–583.

Akinyemi, F. O., Hutchinson, S. M., Mîndrescu, M., & Rothwell, J. J. 2013. Lake sediment records of atmospheric pollution in the Romanian Carpathians. Quaternary International, 293, 105-113.

Aloisi, G., Soulet, G., Henry, P., Wallmann, K., Sauvestre, R., Vallet-Coulomb, C., Bard, E., 2015. Freshening of the Marmara Sea prior to its post-glacial reconnection to the Mediterranean Sea. Earth Planet. Sci. Lett. 413, 176–185. http://dx.doi.org/10.1016/j.epsl.2014.12.052.

Alp, H. 2014. Evidence for active faults in Küçükçekmece Lagoon (Marmara Sea, Turkey), inferred from high-resolution seismic data. Geo-Marine Letters, 34(5), 447-455.

Ambraseys, N.N., Finkel, C.F., 1995. The Seismicity of Turkey and Adjacent Areas - A Historical Review. Eren Yayıncılık, Istanbul, pp. 1500–1800. 240 pp.

Armijo, R., Meyer, B., Navarro, S., King, G., & Barka, A. 2002. Asymmetric slip partitioning in the Sea of Marmara pull-apart: A clue to propagation processes of the North Anatolian fault?. Terra Nova, 14(2), 80-86.

677 Ikehara, K., Irino, T., Usami, K., Jenkins, R., Omura, A., & Ashi, J. (2014). Possible submarine
678 tsunami deposits on the outer shelf of Sendai Bay, Japan resulting from the 2011 earthquake
679 and tsunami off the Pacific coast of Tohoku. Marine Geology, 358, 120-127.

680 Avşar, U., Hubert-Ferrari, A., De Batist, M., Schmidt, S., Fagel, N., 2015. Sedimentary records
681 of past earthquakes in Boraboy Lake during the last ca 600 years (North Anatolian Fault,
682 Turkey). Palaeogeography, Palaeoclimatology, Palaeoecology 433, 1–9.

683 Aydoğdu, A., Hoar, T. J., Vukicevic, T., Anderson, J. L., Pinardi, N., Karspeck, A., ... & Özsoy,
684 E. 2018. OSSE for a sustainable marine observing network in the Sea of Marmara. Nonlinear
685 Processes in Geophysics, 25(3), 537-551.

686 Barnes, P.M., Bostock, H.C., Neil, H.L., Strachan, L.J., Gosling, M., 2013. A 2300-year
687 Paleoearthquake record of the Southern Alpine Fault and Fiordland Subduction Zone, New
688 Zealand, based on stacked turbidites. Bulletin of the Seismological Society of America 103 (4),
689 2424–2446.

690 Beck, C. 2009. Late Quaternary lacustrine paleo-seismic archives in north-western Alps:
691 Examples of earthquake-origin assessment of sedimentary disturbances. Earth-Science
692 Reviews, 96(4), 327-344.

693 Beck, C., de Lépinay, B. M., Schneider, J. L., Cremer, M., Çağatay, N., Wendenbaum, E., ... &
694 Jaouen, A. 2007. Late Quaternary co-seismic sedimentation in the Sea of Marmara's deep
695 basins. Sedimentary Geology, 199(1-2), 65-89.

696 Beck, C., Manalt, F., Chapron, E., Van Rensbergen, P., De Batist, M., 1996. Enhanced
697 seismicity in the early post-glacial period: evidence from the post-würm sediments of Lake
698 Annecy, Northwestern Alps. Journal of Geodynamics 22, 155–171.

699 Beşiktepe, Ş.T., Sur, H.I., Özsoy, E., Latif, M.A., Oğuz, T., Ünlüata, Ü., 1994. The circulation
700 and hydrography of the Marmara Sea. Progress in Oceanography 34 (4), 285–334.

701 Blaauw, M., 2010. Methods and code for 'classical' age-modelling of radiocarbon sequences.
702 Quat. Geochronol. 5, 512e518.

703 Bloemendal, J., King, J. W., Hall, F. R., & Doh, S. J. 1992. Rock magnetism of Late Neogene
704 and Pleistocene deep-sea sediments: Relationship to sediment source, diagenetic processes, and
705 sediment lithology. Journal of Geophysical Research: Solid Earth, 97(B4), 4361-4375.

706 Bourry, C., Chazallon, B., Charlou, J.L., Donval, J.P., Ruffine, L., Henry, P., ... Moreau, M.,
707 2009. Free gas and gas hydrates from the Sea of Marmara, Turkey: chemical and structural
708 characterization. Chemical Geology 264 (1–4), 197–206.

709 Çağatay, M. N., & Uçarkuş, G. 2019. Morphotectonics of the Sea of Marmara: basins and highs
710 on the North Anatolian continental transform plate boundary. In Transform plate boundaries
711 and fracture zones (pp. 397-416). Elsevier.

712 Çağatay, M. N., Eriş, K. K., Makaroğlu, Ö., Yakupoğlu, N., Henry, P., Leroy, S. A., ... & Kende,
713 J. 2019. The sea of Marmara during marine isotope stages 5 and 6. Quaternary Science Reviews,
714 220, 124-141.

715 Çağatay, M. N., Görür, N., Algan, O., Eastoe, C., Tchapalyga, A., Ongan, D., ... & Kuşcu, I.
716 2000. Late Glacial–Holocene palaeoceanography of the Sea of Marmara: timing of connections
717 with the Mediterranean and the Black Seas. Marine Geology, 167(3-4), 191-206.

718 Çağatay, M.N., Algan, O., Sakınç, M., Eastoe, C., Egesel, L., Balkıs, N., Ongan, D., Caner, H.,
719 1999. A mid-late Holocene sapropelic sediment unit from the Southern Marmara shelf and its
720 Paleoenvironmental significance. Quaternary Science Reviews 18, 531–540.

721 Çağatay, M.N., Erel, L., Bellucci, L.G., Polonia, A., Gasperini, L., Eris, K., Sancar, Ü., Biltekin,
722 D., Uçarkus, G., Ülgen, U.B., Damci, E., 2012. Sedimentary earthquake records in the Izmit
723 Gulf, Sea of Marmara, Turkey. Sedimentary Geology 282, 347–359.
724 https://doi.org/10.1016/j.sedgeo.2012.10.001.

725 Çağatay, M.N., Eriş, K., Ryan, W.B.F., Sancar, Ü., Polonia, A., Akçer, S., ... Bard, E., 2009.
726 Late Pleistocene–Holocene evolution of the northern shelf of the Sea of Marmara. Marine
727 Geology 265 (3–4), 87–100.

728 Çağatay, M.N., Görür, N., Polonia, A., Demirbağ, E., Sakınç, M., Cormier, M.H., ... Eriş, K.,
729 2003. Sea-level changes and depositional environments in the Izmit Gulf, eastern Marmara Sea,
730 during the late glacial–Holocene period. Marine Geology 202 (3–4), 159–173.

731 Çağatay, M.N., Wulf, S. Guichard, F. Özmaral, A., Henry, P, Gasperini, L., 2015. Tephra record
732 from the Sea of Marmara for the last 71 ka and its paleoceanographic implications. Marine
733 Geology, 361: 96-110.

734 Çağatay, N., Görür, N., Algan, O., Eastoe, C.J., Tchapalyga, A., Ongan, D., ... Kuscu, I., 2000.
735 Late Glacial-Holocene paleoceanography of the Marmara Sea: timing of connections with the
736 Mediterranean and the Black Seas. Marine Geology 167, 191–206.

737 Campos, C., Beck, C., Crouzet, C., Demory, F., Van Welden, A., & Eris, K. 2013. Deciphering
738 hemipelagites from homogenites through anisotropy of magnetic susceptibility. Paleoseismic
739 implications (Sea of Marmara and Gulf of Corinth). Sedimentary Geology, 292, 1-14.

740 Caner, H. and O. Algan, 2002. Palynology of sapropelic layers from the Marmara Sea. Marine
741 Geology, 190: 35–46.

742 Chapron, E., Beck, C., Pourchet, M., & Deconinck, J. F. 1999. 1822 earthquake-triggered
743 homogenite in Lake Le Bourget (NW Alps). Terra Nova, 11(2-3), 86-92.

744 Chiggiato, J., Jarosz, E., Book, J. W., Dykes, J., Torrisi, L., Poulain, P. M., ... & Beşiktepe, Ş.
745 2012. Dynamics of the circulation in the Sea of Marmara: numerical modeling experiments and
746 observations from the Turkish straits system experiment. Ocean Dynamics, 62(1), 139-159.

747 Cita, M. B., & Rimoldi, B. 1997. Geological and geophysical evidence for a holocene tsunami
748 deposit in the eastern Mediterranean deep-sea record. Journal of Geodynamics, 24(1-4), 293-
749 304.

750 Cita,M.B., Aloisi, G., 2000. Deep-sea tsunami deposits triggered by the explosion of Santorini
751 (3500 a BP), Eastern Mediterranean. Sedimentary Geology 135, 181–203.

752 Dalgıç, S. 2004. Factors affecting the greater damage in the Avcılar area of Istanbul during the
753 17 August 1999 Izmit earthquake. Bulletin of Engineering Geology and the Environment,
754 63(3), 221-232.

755 Demory, F., Nowaczyk, N. R., Witt, A., & Oberhänsli, H. 2005a. High-resolution
756 magnetostratigraphy of late quaternary sediments from Lake Baikal, Siberia: timing of
757 intracontinental paleoclimatic responses. Global and Planetary Change, 46(1-4), 167-186.

758 Demory, F., Oberhänsli, H., Nowaczyk, N. R., Gottschalk, M., Wirth, R., & Naumann, R.
759 2005b. Detrital input and early diagenesis in sediments from Lake Baikal revealed by rock
760 magnetism. Global and Planetary Change, 46(1-4), 145-166.

761 Drab, L., Carlut, J., Hubert-Ferrari, A., Martinez, P., Lepoint, G., & El Ouahabi, M. 2015a.
762 Paleomagnetic and geochemical record from cores from the Sea of Marmara, Turkey: Age
763 constraints and implications of sapropelic deposition on early diagenesis. Marine Geology, 360,
764 40-54.

765 Drab, L., Hubert-Ferrari, A., Schmidt, S., Martinez, P., 2012. The earthquake record in the
766 western part of the Sea of Marmara, Turkey. In: Pantosi, D. (Ed.), Natural Hazards and Earth

System Sciences, Special Issue “Subaqueous Paleoseismology”, pp. 1235–1254 https://doi.org/10.5194/nhess-12-2012.

Drab, L., Hubert-Ferrari, A., Schmidt, S., Martinez, P., Carlut, J., El Ouahabi, M., 2015b. Submarine earthquake history of the Çınarcık segment of the North Anatolian Fault in the Marmara Sea, Turkey. Bulletin of the Seismological Society of America 105 (2A), 622–645.

EIE, 1993. Sediment data and sediment transport amounts for surface waters in Turkish rivers. EIE, Ankara, Rep Gen. Dir. State Electric Serv. 93e59.

Eriş, K. K., Çağatay, M. N., Akçer, S., Gasperini, L., & Mart, Y. 2011. Late glacial to Holocene sea-level changes in the Sea of Marmara: new evidence from high-resolution seismics and core studies. Geo-Marine Letters, 31(1), 1-18.

Eriş, K. K., Ryan, W. B. F., Çağatay, M. N., Sancar, U., Lericolais, G., Menot, G., & Bard, E. 2007. The timing and evolution of the post-glacial transgression across the Sea of Marmara shelf south of Istanbul. Marine Geology, 243(1-4), 57-76.

Eriş, K. K., Sabuncu, A., Gasperini, L., Polonia, A., & Kındap, T. 2019. Influence of climate on the late Pleistocene depositional history of the Gulf of Gemlik (Sea of Marmara). Geo-Marine Letters, 39(3), 205-221.

Eriş, K.K., Çağatay, N., Beck, C., Mercier de Lepinay, B., Campos, C., 2012. Late-Pleistocene to Holocene sedimentary fills of the Cinarcik Basin of the Sea of Marmara. Sedimentary Geology 281, 151–165.

Filikci, B., Eriş, K. K., Çağatay, N., Sabuncu, A., & Polonia, A. 2017. Late glacial to Holocene water level and climate changes in the Gulf of Gemlik, Sea of Marmara: evidence from multi-proxy data. Geo-Marine Letters, 37(5), 501-513.

789 Flerit, F., Armijo, R., King, G. C. P., Meyer, B., & Barka, A. 2003. Slip partitioning in the Sea
790 of Marmara pull-apart determined from GPS velocity vectors. Geophysical Journal
791 International, 154(1), 1-7.

792 Franke, C., Kissel, C., Robin, E., Bonté, P., & Lagroix, F. 2009. Magnetic particle
793 characterization in the Seine river system: Implications for the determination of natural versus
794 anthropogenic input. Geochemistry, Geophysics, Geosystems, 10(8).

795 Gastineau, R., de Sigoyer, J., Sabatier, P., Fabbri, S. C., Anselmetti, F. S., Develle, A. L., ... &
796 Gebhardt, A. C. 2021. Active subaquatic fault segments in Lake Iznik along the middle strand
797 of the North Anatolian Fault, NW Turkey. Tectonics, 40(1), e2020TC006404.

798 Ge, S., Shi, X., Liu, Y., Wang, K., Zou, J., Diao, J., ... & Wang, C. 2012. Turbidite and bottom-
799 current evolution revealed by anisotropy of magnetic susceptibility of redox sediments in the
800 Ulleung Basin, Sea of Japan. Chinese Science Bulletin, 57(6), 660-672.

801 Gibbs, R.J., 1983. Coagulation rates of clay minerals and natural sediments. Journal of
802 Sedimentary Research) 53 (4): 1193–1203. https://doi.org/10.1306/212F8341-2B24-11D7-
803 8648000102C1865D.

804 Goldfinger, C., 2011. Submarine paleoseismology based on turbidite records. Annual Review
805 of Marine Science 3, 35–66.

806 Goldfinger, C., Galer, S., Beeson, J., Hamilton, T., Black, B., Romsos, C., ... Morey, A., 2017.
807 The importance of site selection, sediment supply, and hydrodynamics: a case study of
808 submarine paleoseismology on the Northern Cascadia margin, Washington USA. Marine
809 Geology 384, 4–46.

810 Goldfinger, C., Grijalva, K., Burgmann, K., Morey, A., Johnson, J.E., Nelson, C.H., Gutiérrez-
811 Pastor, J., Karabanov, E., Patton, J., Gracia, E., 2008. Late Holocene rupture of the northern

812 San Andreas Fault and possible stress linkage to the Cascadia Subduction Zone. Seismological
813 Society of America, Bulletin 98, 861–899.

814 Goldfinger, C., Morey, A.E., Nelson, C.H., Gutierrez-Pastor, J., Johnson, J.E., et al., 2007.
815 Rupture lengths and temporal history of significant earthquakes on the offshore and north coast
816 segments of the northern San Andreas Fault based on turbidite stratigraphy. Earth and Planetary
817 Science Letters 254, 9–27.

818 Goldfinger, C., Nelson, C.H., Johnson, J.E., 2003. Holocene earthquake records from the
819 Cascadia subduction zone and northern San Andreas fault based on precise dating of offshore
820 turbidites. Annual Review of Earth and Planetary Sciences 31, 555–577.

821 Gorsline, D. S., De Diego, T., & Nava-Sanchez, E. H. 2000. Seismically triggered turbidites in
822 small margin basins: Alfonso Basin, western Gulf of California and Santa Monica Basin,
823 California borderland. Sedimentary Geology, 135(1-4), 21-35.

824 Grant, K. M., Rohling, E. J., Bar-Matthews, M., Ayalon, A., Medina-Elizalde, M., Ramsey, C.
825 B., Roberts, A. P. 2012. Rapid coupling between ice volume and polar temperature over the
826 past 150,000 years. Nature, 491(7426), 744-747.

827 Gutiérrez-Pastor, J., Nelson, C.H., Goldfinger, C., Escutia, C., 2013. Sedimentology of seismo-
828 turbidites off the Cascadia and northern California active tectonic continental margins,
829 northwest Pacific Ocean. Marine Geology 336, 99–119.

830 Harrison, C. G. A., & Funnell, B. M. 1964. Relationship of palaeomagnetic reversals and
831 micropalaeontology in two late Caenozoic cores from the Pacific Ocean. Nature, 204(4958),
832 566-566.

833 Henry, H., Özeren, M.S., Yakupoğlu, N., Çakir, Z., De Saint-Léger, E., De Gésincourt, O.D.,
834 Tengberg, A., Chevalier, C., Papoutsellis, C., Postacıoğlu, N. Dogan, U., Karabulut, K.,

Uçarkuş G., Çağatay, M.N. 2022. Slow build-up of turbidity currents triggered by a moderate earthquake in the Sea of Marmara. Natural hazards and Earth System Sciences. https://doi.org/10.5194/nhess-2021-323.

Hiscott, R. N., Hall, F. R., & Pirmez, C. 1997. Turbidity-current overspill from the Amazon Channel: texture of the silt/sand load, paleoflow from anisotropy of magnetic susceptibility, and implications for flow processes. In Proceedings-Ocean Drilling Program Scientific Results (pp. 53-78). NATIONAL SCIENCE FOUNDATION.

Howarth, J. D., Orpin, A. R., Kaneko, Y., Strachan, L. J., Nodder, S. D., Mountjoy, J. J., ... & Cağatay, M. N. 2021. Calibrating the marine turbidite palaeoseismometer using the 2016 Kaikōura earthquake. Nature Geoscience, 14(3), 161-167.

Hrouda, F. 1982. Magnetic anisotropy of rocks and its application in geology and geophysics. Geophysical surveys, 5(1), 37-82.

Ikehara, K., Kanamatsu, T., Nagahashi, Y., Strasser, M., Fink, H., Usami, K., et al. 2016. Documenting large earthquakes similar to the 2011 Tohoku-oki earthquake from sediments deposited in the Japan Trench over the past 1500 years. Earth and Planetary Science Letters, 445, 48–56. doi:10.1016/j.epsl.2016.04.009.

Ikehara, K., Usami, K., Kanamatsu, T., Danhara, T., & Yamashita, T. 2017. Three important Holocene tephras off the Pacific coast of the Tohoku region, Northeast Japan: Implications for correlating onshore and offshore event deposits. Quaternary International, 456, 138–153. doi:10.1016/j.quaint.2017.08.022.

Ikehara, K., Usami, K., & Kanamatsu, T. (2020). Repeated occurrence of surface-sediment remobilization along the landward slope of the Japan Trench by great earthquakes. Earth, Planets and Space, 72(1), 1-9.

858 Jelinek, V. 1981. Characterization of the magnetic fabric of rocks. Tectonophysics, 79(3-4),
859 T63-T67.

860 Johnson, H. P., Lowrie, W., & Kent, D. V. 1975. Stability of anhysteretic remanent
861 magnetization in fine and coarse magnetite and maghemite particles. Geophysical Journal
862 International, 41(1), 1-10.

863 Kastens, K., Cita, M.B., 1981. Tsunami-induced sediment transport in the abyssal
864 Mediterranean Sea. Geological Society of America Bulletin 119, 151–165.

865 Kazancı, N., Leroy, S., Ileri, Ö., Emre, Ö., Kibar, M., & Öncel, S. 2004. Late Holocene erosion
866 in NW Anatolia from sediments of Lake Manyas, Lake Ulubat and the southern shelf of the
867 Marmara Sea, Turkey. Catena, 57(3), 277-308.

868 Kopf, A. Clennell, M.B. , Flecker, R. 1998. Relationship between the variation of undrained
869 shear strength, organic carbon content, and the origin and frequency of enigmatic normal faults
870 in fine-grained sediments from advanced piston cores from the eastern Mediterranean. In:
871 Robertson, A.H.F., Emeis, K.-C., Richter, C., and Camerlenghi, A. (Eds.), Proceedings of the
872 Ocean Drilling Program, Scientific Results, Vol. 160, Chapter 49, pp.655-661.

873 Kruiver, P. P., Kok, Y. S., Dekkers, M. J., Langereis, C. G., & Laj, C. 1999. A pseudo-Thellier
874 relative palaeointensity record, and rock magnetic and geochemical parameters in relation to
875 climate during the last 276 kyr in the Azores region. Geophysical Journal International, 136(3),
876 757-770.

877 Le Pichon, X., Şengör, A. M. C., Demirbağ, E., Rangin, C., Imren, C., Armijo, R., ... & Tok,
878 B. 2001. The active main Marmara fault. Earth and Planetary Science Letters, 192(4), 595-616.

879 Major, C. O., Goldstein, S. L., Ryan, W. B., Lericolais, G., Piotrowski, A. M., & Hajdas, I.
880 2006. The co-evolution of Black Sea level and composition through the last deglaciation and
881 its paleoclimatic significance. Quaternary Science Reviews, 25(17-18), 2031-2047.

882 McClusky, S., Balassanian, S., Barka, A., Demir, C., Ergintav, S., Georgiev, I., ... & Veis, G.
883 2000. Global Positioning System constraints on plate kinematics and dynamics in the eastern
884 Mediterranean and Caucasus. Journal of Geophysical Research: Solid Earth, 105(B3), 5695-
885 5719.

886 McHugh, C.M., Braudy, N., Çağatay, M.N., Sorlien, C., Cormier, M.H., Seeber, L., Henry, P.,
887 2014. Seafloor fault ruptures along the North Anatolia Fault in the Marmara Sea, Turkey: link
888 with the adjacent basin turbidite record. Marine Geology 353, 65–83.

889 McHugh, C.M., Seeber, L., Braudy, N., Cormier, M.-H., Davis, M.B., Diebold, J.B.,
890 Dieudonne, N., Douilly, R., Gulick, S.P.S., Hornbach, M.J., Johnson III, H.E., Ryan, K.M.,
891 Sorlien, C.C., Steckler, M.S., Symithe, S.J., Templeton, J., 2011. Offshore sedimentary effects
892 of the 12 January 2010 Haiti earthquake. Geology 39, 723–726.

893 McHugh, C.M.G., Seeber, L., Cormier, M.-H., Dutton, J., Çağatay, N., Polonia, A., Ryan,
894 W.B.F., Görür, N., 2006. Submarine earthquake geology along the North Anatolia Fault in the
895 Marmara Sea, Turkey: a model for transform basin sedimentation. Earth and Planetary Science
896 Letters 248, 661–684.

897 Moernaut, J., Van Daele, M., Heirman, K., Fontijn, K., Strasser, M., Pino, M., ... & De Batist,
898 M. 2014. Lacustrine turbidites as a tool for quantitative earthquake reconstruction: New
899 evidence for a variable rupture mode in south central Chile. Journal of Geophysical Research:
900 Solid Earth, 119(3), 1607-1633.

901 Moernaut, J., Van Daele, M., Strasser, M., Clare, M. A., Heirman, K., Viel, M., ... & De Batist,
902 M. 2017. Lacustrine turbidites produced by surficial slope sediment remobilization: a

903 mechanism for continuous and sensitive turbidite paleoseismic records. Marine Geology, 384,
904 159-176.

905 Mudie, P.J., A. Rochon, and A.E. Aksu, 2002. Pollen stratigraphy of Late Quaternary cores
906 from Marmara Sea: land–sea correlation and paleoclimatic history. Marine Geology, 190: 233–
907 260.

908 Mulder, T., & Syvitski, J. P. 1995. Turbidity currents generated at river mouths during
909 exceptional discharges to the world oceans. The Journal of Geology, 103(3), 285-299.

910 Nakajima, T., Kanai, Y., 2000. Sedimentary features of seismoturbidites triggered by the 1983
911 and older historical earthquakes in the eastern margin of the Japan Sea. Sedimentary Geology
912 135, 1–19.

913 Nemec, W. 1990. Aspects of sediment movement on steep delta slopes. Coarse-grained deltas,
914 10(2), 29-73.

915 Nizou, J., Demory, F., & Dubrulle-Brunaud, C. 2016. Monitoring of dredged-dumped sediment
916 dispersal off the Bay of the Seine (northern France) using environmental magnetism. Comptes
917 Rendus Geoscience, 348(6), 451-461.

918 Obuka, V. Šinka, M., Kļaviņš, M., Stankeviča, K., Korjakins, A., 2015. Sapropel as a Binder:
919 Properties and Application Possibilities for Composite Materials IOP Conf. Ser.: Mater. Sci.
920 Eng. 96 012026. https://iopscience.iop.org/article/10.1088/1757-899X/96/1/012026.

921 Opdyke, N. D., Glass, B., Hays, J. D., & Foster, J. 1966. Paleomagnetic study of Antarctic
922 deep-sea cores. Science, 154(3747), 349-357.

923 Parsons, T., 2004. Recalculated probability of M>7 earthquakes beneath the Sea of Marmara.
924 Journal of Geophysical Research., 109, doi:10.1029/2003JB002667.

925 Patton, J. R., Goldfinger, C., Morey, A. E., Ikehara, K., Romsos, C., Stoner, J., ... & Vizcaino,
926 A. (2015). A 6600 year earthquake history in the region of the 2004 Sumatra-Andaman
927 subduction zone earthquake. Geosphere, 11(6), 2067-2129.

928 Petersen, J., Wilhelm, B., Revel, M., Rolland, Y., Crouzet, C., Arnaud, F., ... & Magand, O.
929 2014. Sediments of Lake Vens (SW European Alps, France) record large-magnitude earthquake
930 events. Journal of paleolimnology, 51(3), 343-355.

931 Polonia, A., Nelson, C.H., Romano, S., Vaiani, S.C., Colizza, E., Gasparotto, G., Gasperini, L.,
932 2017. A depositional model for seismo-turbidites in confined basins based on Ionian Sea
933 deposits. Marine Geology 384, 177–198.

934 Polonia, A., Panieri, G., Gasperini, L., Gasparotto, G., Bellucci, L.G., Torelli, L., 2013.
935 Turbidite paleoseismology in the Calabrian Arc subduction complex (Ionian Sea).
936 Geochemistry, Geophysics, Geosystems 14, 112–140. https://doi.org/10.1029/2012GC004402.

937 Pouderoux, H., Lamarche, G., Proust, J.-N., 2012b. Building a 18 000-year-long
938 paleoearthquake record from detailed deep-sea turbidite characterisation in Poverty Bay, New
939 Zealand. Natural Hazards and Earth System Sciences 12, 1–25.

940 Pouderoux, H., Proust, J.N., Lamarche, G., Orpin, A., Neil, H., 2012a. Deep-sea sedimentation
941 along the Hikurangi subduction margin (New Zealand) since the Last Glacial Maximum:
942 characterisation, timing and origin of turbidites. Marine Geology 295e298, 51–76.

943 Pozza, M. R., Boyce, J. I., & Morris, W. A. 2004. Lake-based magnetic mapping of
944 contaminated sediment distribution, Hamilton Harbour, Lake Ontario, Canada. Journal of
945 Applied Geophysics, 57(1), 23-41.

946 Prior, D. B., Suhayda, J. N., Lu, N. Z., Bornhold, B. D., Keller, G. H., Wiseman, W. J., ... &
947 Yang, Z. S. 1989. Storm wave reactivation of a submarine landslide. Nature, 341(6237), 47-50.

948 Provost, A.S., Chéry, J., Hassani, R., 2003. 3D mechanical modeling of the GPS velocity field
949 along the North Anatolian fault. Earth and Planetary Science Letters 209 (3–4), 361–377.

950 Rapuc W., Sabatier P., Andric M., Crouzet C., Arnaud F., Smuc A., Chapron E., Develle A.-
951 L., Wilhelm B., Demory F., Reyss J.-L., Régnier E., Daut G., Von Grafenstein U. 2018.
952 Evolution of the local seismicity during the Holocene recorded in Bohinj's lacustrine sediments
953 (Slovenia). *Sedimentology*, 65-5, 1777-1799. http://dx.doi.org/10.1111/sed.12446

954 Reilinger, R. E., McClusky, S. C., Oral, M. B., King, R. W., Toksoz, M. N., Barka, A. A., ... &
955 Sanli, I. 1997. Global Positioning System measurements of present-day crustal movements in
956 the Arabia-Africa-Eurasia plate collision zone. Journal of Geophysical Research: Solid Earth,
957 102(B5), 9983-9999.

958 Reilinger, R., McClusky, S., Vernant, P., Lawrence, S., Ergintav, S., Cakmak, R., ... & Karam,
959 G. 2006. GPS constraints on continental deformation in the Africa-Arabia-Eurasia continental
960 collision zone and implications for the dynamics of plate interactions. Journal of Geophysical
961 Research: Solid Earth, 111(B5).

962 Reimer, P. J., Bard, E., Bayliss, A., Beck, J. W., Blackwell, P. G., Ramsey, C. B., ... & Van Der
963 Plicht, J. 2013. IntCal13 and Marine13 radiocarbon age calibration curves 0–50,000 years cal
964 BP. radiocarbon, 55(4), 1869-1887.

965 Rochette, P., Jackson, M., & Aubourg, C. 1992. Rock magnetism and the interpretation of
966 anisotropy of magnetic susceptibility. Reviews of Geophysics, 30(3), 209-226.

967 Ryan, W. B. 2007. Status of the Black Sea flood hypothesis. In The Black Sea Flood Question:
968 Changes in Coastline, Climate, and Human Settlement (pp. 63-88). Springer, Dordrecht.

969 Sarı, E., Çağatay,M.N., 2006. Turbidities and their association with past earthquakes in the deep
970 Çınarcık Basin of the Marmara Sea. Geo-Marine Letters 26, 69–76.

971 Şengör, A. M. C., Tüysüz, O., Imren, C., Sakınç, M., Eyidoğan, H., Görür, N., ... & Rangin, C.
972 2005. The North Anatolian fault: A new look. Annu. Rev. Earth Planet. Sci., 33, 37-112.

973 Shiki, T., Kumon, F., Inouchi, Y., Kontani, Y., Sakamoto, T., Tateishi, M., Matsubara, H.,
974 Fukuyama, K., 2000. Sedimentary features of the seismo-turbidites, Lake Biwa, Japan.
975 Sedimentary Geology 135, 37–50.

976 Siani, G., Paterne, M., Arnold, M., Bard, E., Métivier, B., Tisnerat, N., & Bassinot, F. 2000.
977 Radiocarbon reservoir ages in the Mediterranean Sea and Black Sea. Radiocarbon, 42(2), 271-
978 280.

979 Stachowska, A., Łoziński, M., Śmigielski, M., Wysocka, A., Jankowski, L., & Ziółkowski, P.
980 2020. Anisotropy of magnetic susceptibility as an indicator for palaeocurrent analysis in folded
981 turbidites (Outer Western Carpathians, Poland). Sedimentology, 67(7), 3783-3808.

982 Stoner, J. S., & St-Onge, G. 2007. Chapter three magnetic stratigraphy in paleoceanography:
983 reversals, excursions, paleointensity, and secular variation. Developments in Marine
984 Geology, 1, 99-138.

985 Straub, C., Kahle, H. G., & Schindler, C. 1997. GPS and geologic estimates of the tectonic
986 activity in the Marmara Sea region, NW Anatolia. Journal of Geophysical Research: Solid
987 Earth, 102(B12), 27587-27601.

988 Tamaki, M., Suzuki, K., & Fujii, T. 2015. Paleocurrent analysis of Pleistocene turbidite
989 sediments in the forearc basin inferred from anisotropy of magnetic susceptibility and
990 paleomagnetic data at the gas hydrate production test site in the eastern Nankai Trough. Marine
991 and Petroleum Geology, 66, 404-417.

992 Tarling, D., & Hrouda, F. (Eds.). 1993. Magnetic anisotropy of rocks. Springer Science &
993 Business Media.

994 Tolun, T., Çağatay, M.N., Carrigan, W.J., 2002. Organic geochemistry and origin of Holocene
995 sapropelic layer and associated sediments in Marmara Sea. Marine Geology 190, 47–60.

996 Uçarkuş, G., 2010. Active Faulting and Earthquake Scarps a Long the North Anatolian Fault in
997 The Sea of Marmara (Doctoral dissertation, Avrasya Yer Bilimleri Enstitüsü).

998 Ünlülata, Ü., Oğuz, T., Latif, M.A., Özsoy, E., 1990. On the physical oceanography of the
999 Turkish Straits. The Physical Oceanography of Sea Straits. Springer, Dordrecht, pp. 25–60.

1000 Valsecchi, V., M.F. Sánchez-Goñi, and L. Londeix, 2012. Vegetation dynamics in the
1001 Northeastern Mediterranean region during the past 23 000 yr: insights from a new pollen record
1002 from the Sea of Marmara. Clim. Past, 8: 1941–1956.

1003 Van Daele, M., Meyer, I., Moernaut, J., De Decker, S., Verschuren, D., & De Batist, M. 2017.
1004 A revised classification and terminology for stacked and amalgamated turbidites in
1005 environments dominated by (hemi) pelagic sedimentation. Sedimentary Geology, 357, 72-82.

1006 Vidal, L., Ménot, G., Joly, C., Bruneton, H., Rostek, F., Çağatay, M.N., Major, M., Bard, E.,
1007 2010. Hydrology in the Sea of Marmara during the last 23 ka: implications for timing of Black
1008 Sea connections and sapropel deposition. Paleoceanography 25 (1), pa1205.
1009 http://dx.doi.org/10.1029/2009pa001735.

1010 Wilhelm, B., Nomade, J. , Crouzet, C. , Litty, C., Sabatier, P., Belle, S., Rolland, Y., Revel, M.,
1011 Courboulex, F., Arnaud, F., Anselmetti, F.S., 2016. Quantified sensitivity of small lake
1012 sediments to record historic earthquakes: Implications for paleoseismology, J. Geophys. Res.
1013 Earth Surf., 121, 2–16, http://doi:10.1002/2015JF003644.

1014 Wilkinson, K.J. Negre, J.-C., Buffle, J. 1997. Coagulation of colloidal material in surface
1015 waters: the role of natural organic matterm Journal of Contaminant Hydrology. 26 (1–4), 229-
1016 243.

Wils, K., Van Daele, M., Kissel, C., Moernaut, J., Schmidt, S., Siani, G., & Lastras, G. 2020. Seismo-Turbidites in Aysén Fjord (Southern Chile) Reveal a Complex Pattern of Rupture Modes Along the 1960 Megathrust Earthquake Segment. Journal of Geophysical Research: Solid Earth, 125(9), e2020JB019405.

Yakupoğlu, N., Uçarkuş, G., Eriş, K. K., Henry, P., & Çağatay, M. N. 2019. Sedimentological and geochemical evidence for seismoturbidite generation in the Kumburgaz Basin, Sea of Marmara: Implications for earthquake recurrence along the Central High Segment of the North Anatolian Fault. Sedimentary Geology, 380, 31-44.

Figure Captions

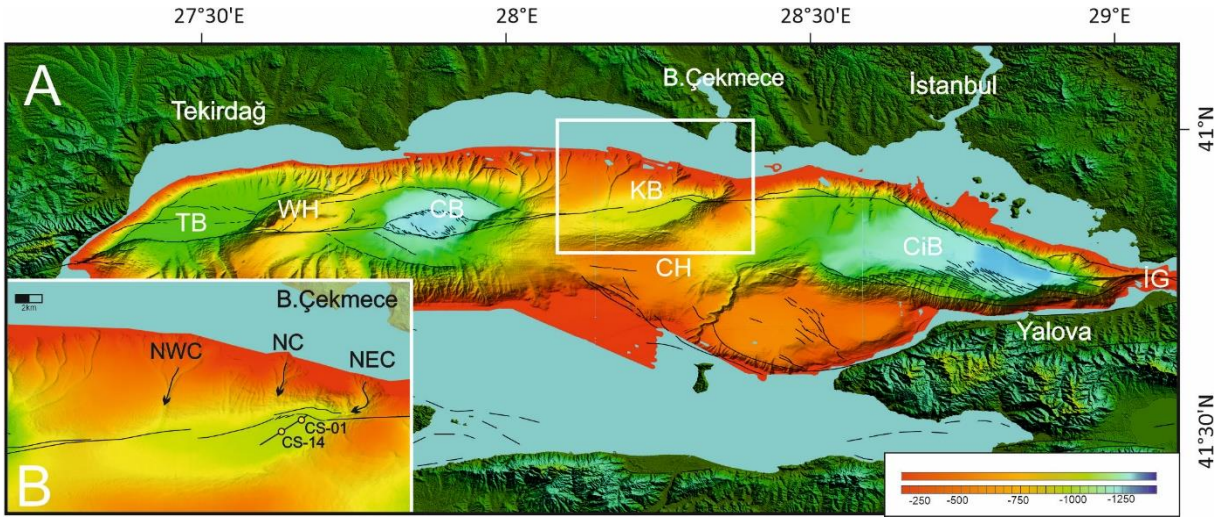

Fig. 1. A) High resolution multi-beam bathymetry map of the Sea of Marmara (west to east; TB: Tekirdağ Basin, WH: Western High, CB: Central Basin, KB: Kumburgaz Basin, CH: Central High, CiB; Çınarcık Basin, GI: Gulf of İzmit) (Revised from Uçarkuş, 2010). Black lines represent the active faults. White box indicates the location of the Kumburgaz Basin and the inset map. B) Close up of bathymetry map of Kumburgaz Basin. Black lines indicate the active faults. Thick black line and yellow dots represents the CHIRP profile (P02) and core locations of CS-01 (Yakupoğlu et al., 2019) and CS-14 (this study) respectively. Note that

northern canyons are indicated as following: NEC: North Eastern Canyon, NE: Northern Canyon, NWC: North Western Canyon.

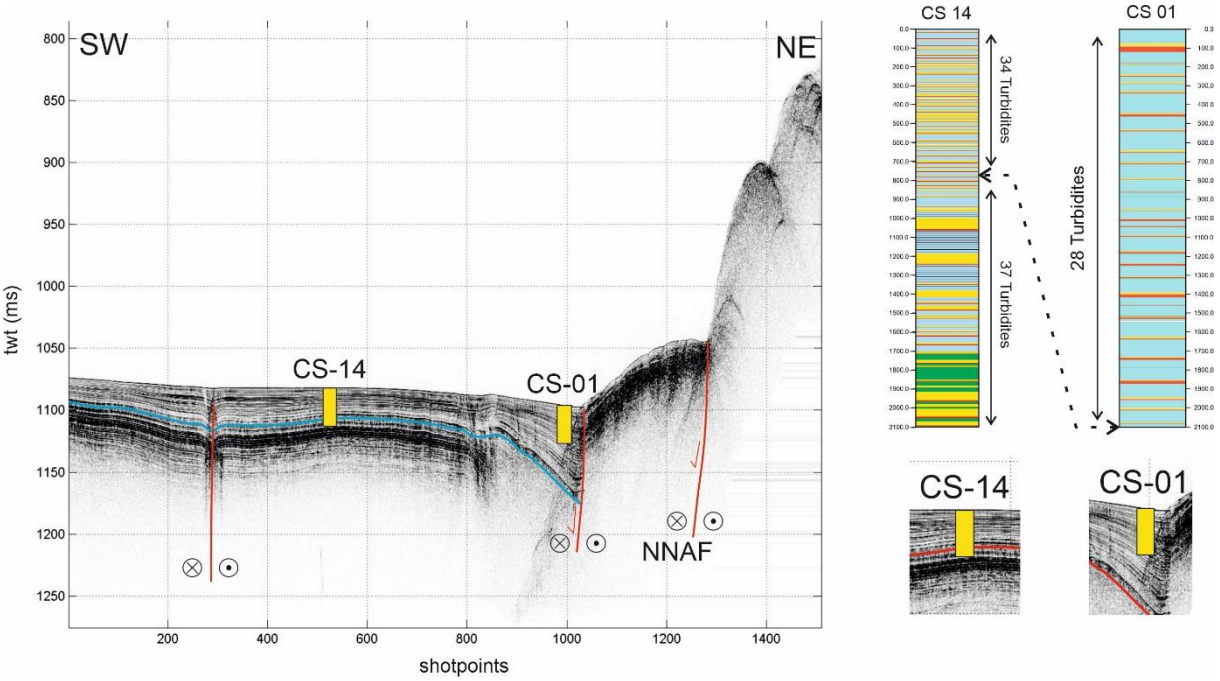

Fig. 2. CHIRP profile (P02) from the Kumburgaz Basin, showing the main depositional units along the basin floor. Lacustrine-Marine transition (12.6 kyrs BP; Çağatay et al., 2015) is shown in blue line. Core CS-01 is located at depocenter covering the last 6 kyrs BP sedimentary records (Yakupoğlu et al., 2019) and Core CS-14 penetrates through lacustrine units of SoM up to 15 cal kyrs BP (Figs. 3, 4).

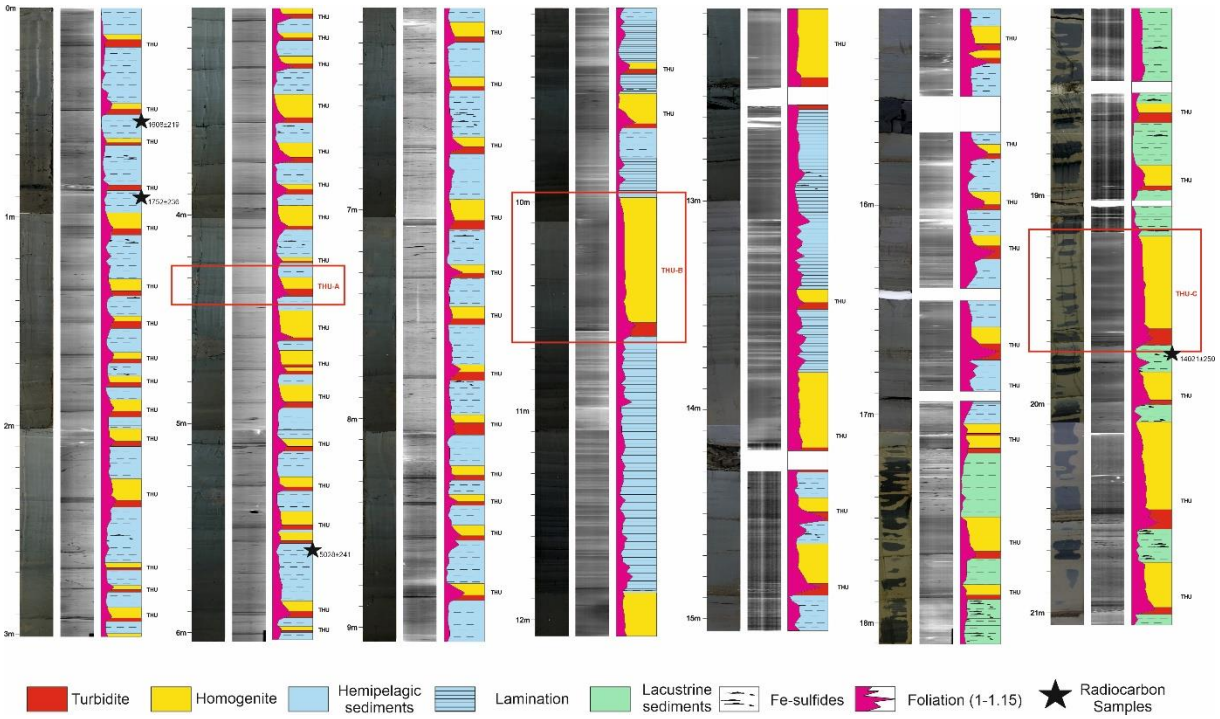

Fig. 3. Generalized lihological log of the core CS-14, showing the main lithostratigraphy photography and radiography of the marine and lacustrine units deposited during the last ~15 cal ka BP (Fig. 4). 70 turbidite layers are differentiated based on sedimentological, geochemical and magnetic precursors. Legend below shows different lithological units and symbols.

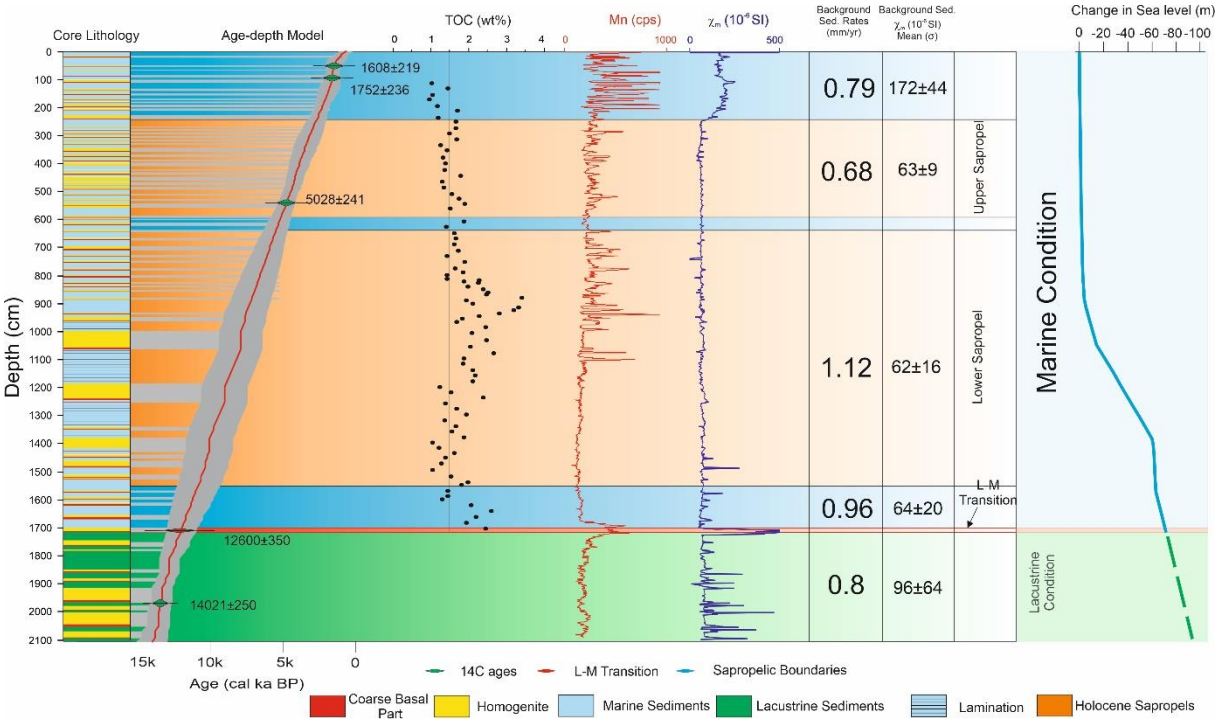

Fig. 4. Age-depth model of the core CS-14. Summarized sedimentary log shows the main lithostratigraphy of the marine and lacustrine units and TOC concentrations of the first 18 m. Age-depth model of the background sediments of the core CS-14 are reconstructed based on four ^{14}C ages and the age of a major lithological change (L-M transition) by using Clam.r Script (Blauuw, 2010). Red line represents the mean age of the iterations. Green, blue and red dots are the levels of the ^{14}C samples, L-M transition respectively. Gray overlay indicates the probability distribution. Mn profile and χ_m profiles are marked in red and blue color respectively. Background sedimentation rates are indicated according to each facies. The rightmost column indicates the climatic phases and global sea level curve of the last 12 kyrs BP (Grant et al., 2012).

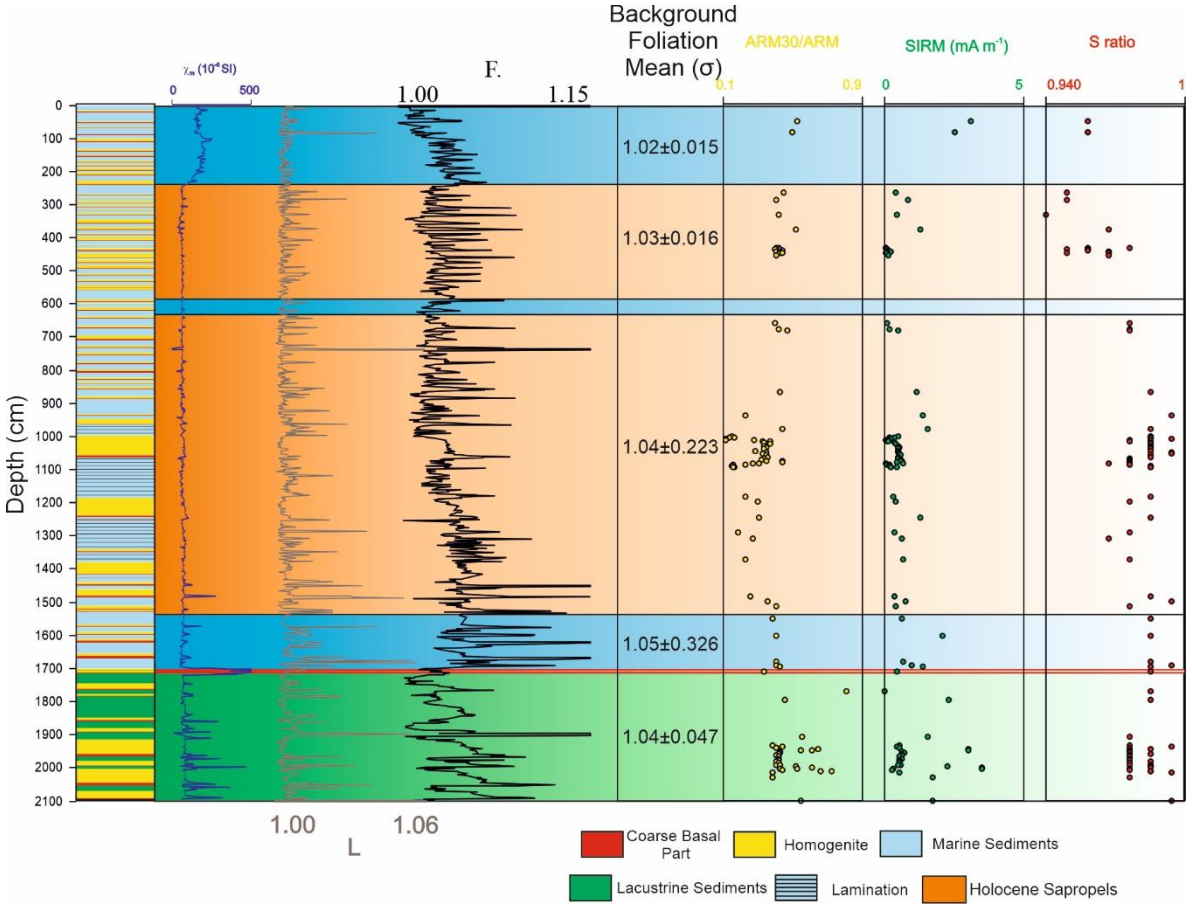

Fig. 5. Summarized sedimentary log of the core accompanied with magnetic foliation, magnetic lineation, S ratio, SIRM, ARM_{30}/ARM profiles of 98 samples showing the rock magnetism proxies.

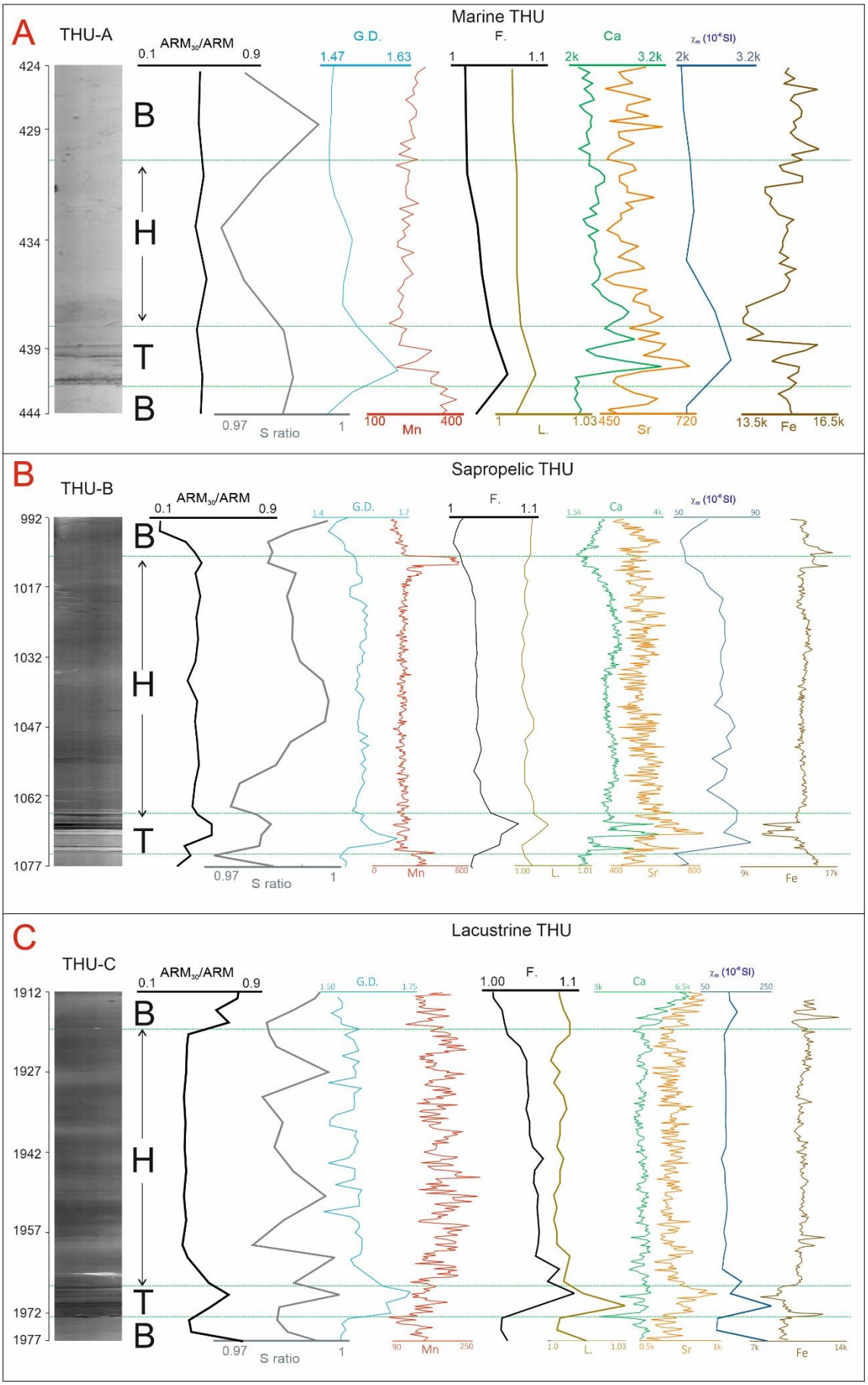
A
THU-A
Marine THU
ARM30/ARM
0.1
0.9
G.D.
1.47
1.63
F.
1
1.1
Ca
2k
3.2k
χm (10-8SI)
2k
3.2k
424
429
434
439
444
B
H
T
B
0.97
S ratio
1
100
Mn
400
1
L.
1.03
450
Sr
720
13.5k
Fe
16.5k
B
THU-B
Sapropelic THU
992
1017
1032
1047
1062
1077
1062

Fig. 6. Radiography and multi-parameter analyses (left to right; ARM_{30}/ARM, S ratio, gamma density, Mn, magnetic foliation and lineation, Ca, Sr, χ_m, Fe) of the selected THUs (THU-A, B, C) (see their positions on Fig 3). Green lines represent the boundary of THU units with background sediments.

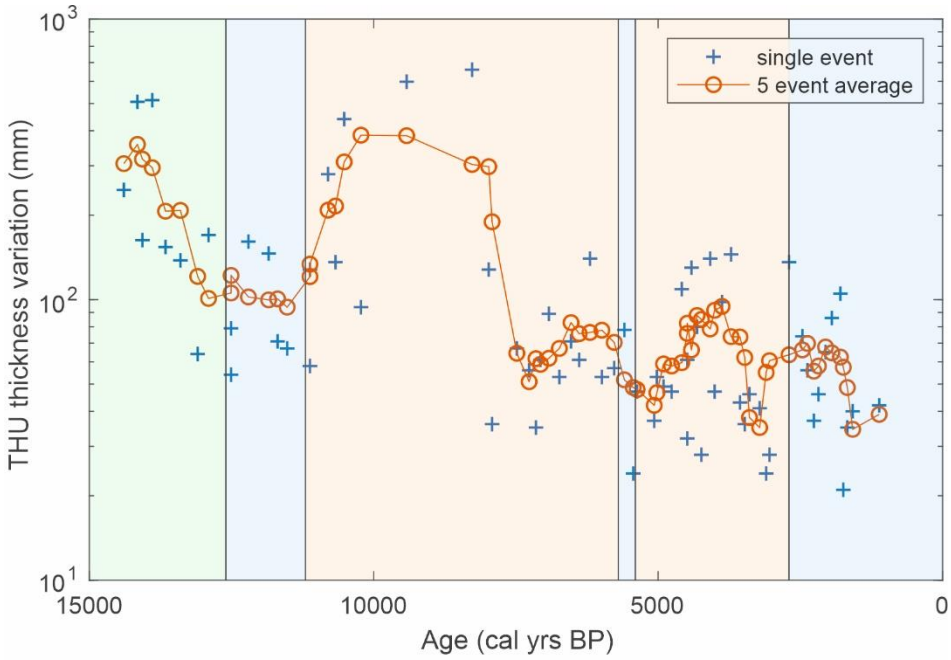
THU thickness variation (mm)
single event
5 event average
Age (cal yrs BP)

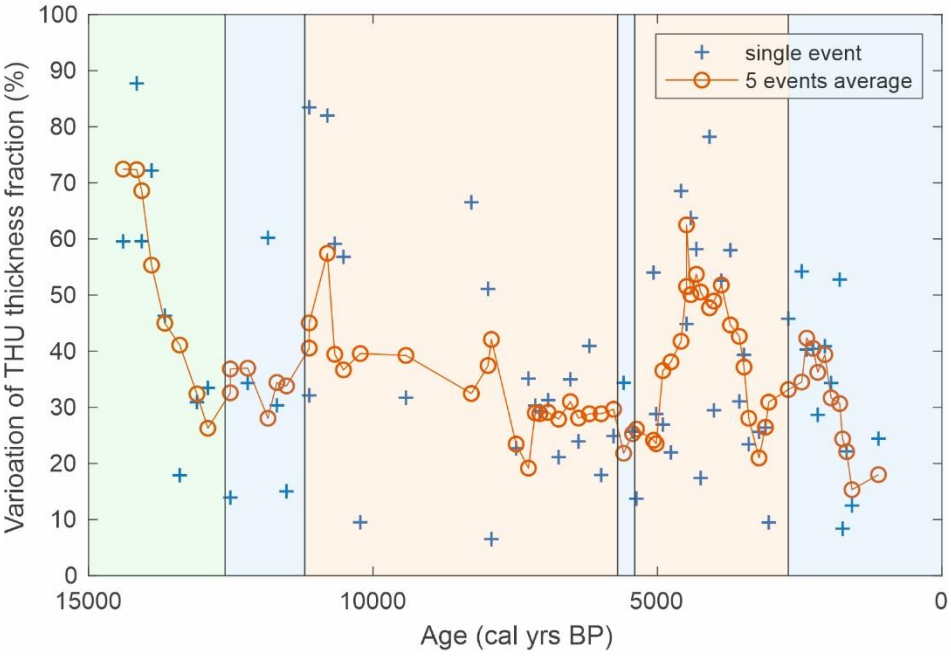
Varioation of THU thickness fraction (%)
single event
5 events average
Age (cal yrs BP)

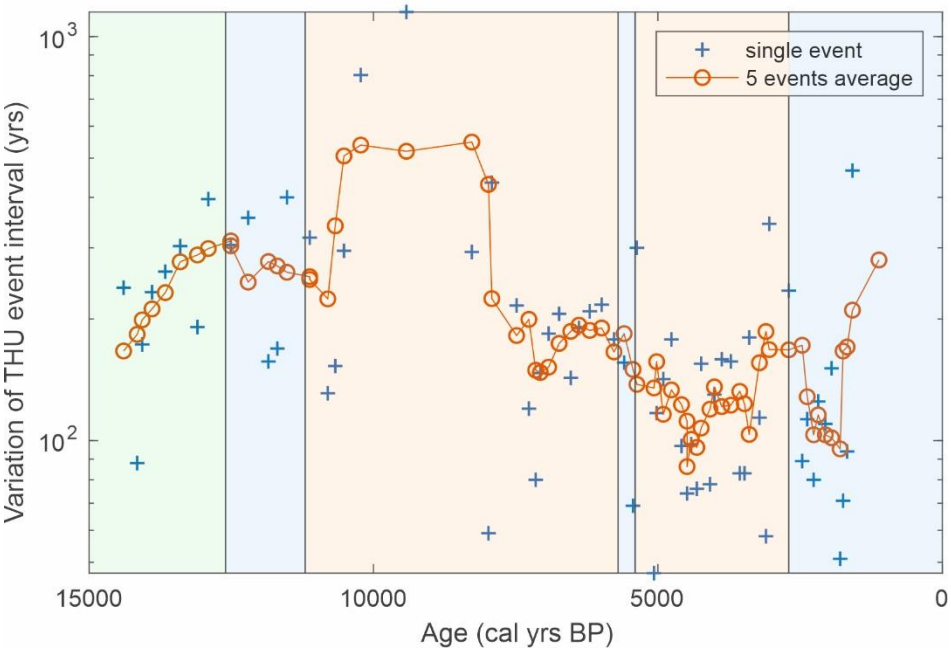
Variation of THU event interval (yrs)
single event
5 events average
Age (cal yrs BP)

1067

Fig. 7. (A) THU thickness variation, (B) Variation of THU thickness fraction, calculated as each THU thickness divided by total sediment thickness between two events, (C) Variation of THU event interval.

Table Captions

Table 1. Summary of Accelerated Mass Spectrometry ^{14}C ages obtained from core CS-14 and the referenced age of full L-M transition (Çağatay et al., 2015). Reservoir correction for Accelerated Mass Spectrometry dates applied as ~390 ± 85 yrs for marine according to Siani et al. (2000) and ~900 ± 100 yrs for lacustrine (Çağatay et al., 2015).

Sample ID	Depth (cm)	Uncalibrated Age (BP)	Calibrated Ages (BP)	Material
TÜBİTAK-675	52	2552±53	1608±219	benthic & planktonic foraminifera, echinoderm spicules
TÜBİTAK-676	92	2432±32	1752±236	benthic & planktonic foraminifera, echinoderm spicules
TÜBİTAK-678	554	5115±40	5028±241	benthic & planktonic foraminifera, echinoderm spicules
TÜBİTAK-794	1984	12538±51	14021±250	Bivalves
Lacustrine-Marine Transition	1740		12600±350 (Çağatay et al., 2015)	

Table 2. THU intervals, frequencies and thicknesses over the lithological facies. Extended list of each unit is displayed on Supplementary Table 1. Note that, standard deviation of THU intervals and thicknesses are indicated in parenthesis.

Unit/Facies	THU intervals (yrs)	THU frequency (kyrs-1)	Background Sedimentation Rate (mm/yr)	Total Sedimentation Rate (mm/yr)	THU thickness (cm)	Percentage of THU (%)	TB/TT ratio

Non-sapropelic Marine	174 (112)	5.747	0.61	0.77	7 (3.9)	30	0.8
Upper Sapropel	114(62)	8.621	0.68	1.29	6.1 (3.6)	38	0.7
Lower Sapropel	287 (254)	3.484	1.12	1.68	15.7 (17.8)	35	0.6
Lacustrine	235(85)	4.255	0.8	1.9	20.8 (16)	53	0.3

Supplementary Table 1. Summary of THU list obtained from the core CS-14. Their depths, facies, thickness, mean ages are listed according to the stratigraphy. Average thicknesses and average recurrence intervals of THUs for each facies, turbidite-homogenite ratios and the background sedimentation rates are listed at the rightmost columns.